



Anatomy of the Indian Summer Monsoon and ENSO relationships in state-of-the-art CGCMs: Role of the tropical Indian Ocean

Pascal Terray, K. P. Sooraj, Sébastien Masson, Chloé Prodhomme

► To cite this version:

Pascal Terray, K. P. Sooraj, Sébastien Masson, Chloé Prodhomme. Anatomy of the Indian Summer Monsoon and ENSO relationships in state-of-the-art CGCMs: Role of the tropical Indian Ocean. Climate Dynamics, 2020, 10.1007/s00382-020-05484-z . hal-03021264

HAL Id: hal-03021264

<https://hal.sorbonne-universite.fr/hal-03021264>

Submitted on 24 Nov 2020

HAL is a multi-disciplinary open access archive for the deposit and dissemination of scientific research documents, whether they are published or not. The documents may come from teaching and research institutions in France or abroad, or from public or private research centers.

L'archive ouverte pluridisciplinaire **HAL**, est destinée au dépôt et à la diffusion de documents scientifiques de niveau recherche, publiés ou non, émanant des établissements d'enseignement et de recherche français ou étrangers, des laboratoires publics ou privés.

Anatomy of the Indian Summer Monsoon and ENSO

relationships in state-of-the-art CGCMs:

Role of the tropical Indian Ocean

Pascal Terray¹, KP Sooraj², Sébastien Masson¹, Chloé Prodhomme³

¹ LOCEAN/IPSL, Sorbonne Universités (UPMC, Univ Paris 06)-CNRS-IRD-MNHN, Paris, France

²CCCR, Indian Institute of Tropical Meteorology, Ministry of Earth Sciences, Pune, India

³UB, Departament de física fonamental, University of Barcelona, Barcelona, Spain

Revised for **Climate Dynamics**

19 August 2020

Corresponding author address: Pascal Terray, LOCEAN-IPSL, Sorbonne Universités (Campus Université Pierre et Marie Curie), BP100 – 4 place Jussieu, 75252 Paris cedex 05, France. Tel : +33 1 44 27 70 72. E-mail : terray@locean-ipsl.upmc.fr

Abstract

Indian Summer Monsoon (ISM) rainfall and El Niño-Southern Oscillation (ENSO) exhibit an inverse relationship during boreal summer, which is one of the roots of ISM interannual variability and its seasonal predictability. Here we document how current climate and seasonal prediction models simulate the timing and amplitude of this ISM-ENSO teleconnection. Many Coupled General Circulation Models (CGCMs) do simulate a simultaneous inverse relationship between ENSO and ISM, though with a large spread. However, most of them show significant negative correlations before ISM, which are at odd with observations. Consistent with this systematic error, simulated Niño-3.4 Sea Surface Temperature (SST) variability has erroneous high amplitude during boreal spring and ISM rainfall variability is also too strong during the first part of ISM.

The role of the Indian Ocean (IO) in modulating the ISM-ENSO relationships is further investigated using dedicated experiments with the SINTEX-F2 CGCM. Decoupled tropical Pacific and IO experiments are conducted to assess the direct relationship between ISM and IO SSTs on one hand, and the specific role of IO feedback on ENSO on the other hand. The direct effect of IO SSTs on ISM is weak and insignificant at the interannual time scale in the Pacific decoupled experiment. On the other hand, IO decoupled experiments demonstrate that El Niño shifts rapidly to La Niña when ocean-atmosphere coupling is active in the whole IO or only in its western part. This IO negative feedback is mostly active during the decaying phase of El Niño, which is accompanied by a basin-wide warming in the IO, and significantly modulates the length of ENSO events in our simulations.

This IO feedback operates through a modulation of the Walker circulation over the IO, which strengthens and shifts eastward an anomalous anticyclone centered on the Philippine Sea and associated easterly wind anomalies in the equatorial western Pacific during boreal winter. In turn, these atmospheric anomalies lead to a fast ENSO turnabout via oceanic adjustment processes mediated by eastward propagating upwelling Kelvin waves. An experiment in which only the SouthEast Indian Ocean (SEIO) is decoupled, demonstrates that the equatorial SST gradient in the IO during boreal winter plays a fundamental role in the efficiency of IO feedback. In this experiment, simulated ISM-ENSO lead-lag correlations match closely the observations. This success is associated with removal of erroneous SEIO SST variability during boreal winter in the SEIO decoupled experiment. Finally, it is illustrated that most CMIP5 CGCMs exhibit similar SST errors in the SEIO during boreal winter in addition to an exaggerated SEIO SST variability during boreal fall.

Keywords: Indian Summer Monsoon; El Niño-Southern Oscillation; Indian Ocean; ocean-atmosphere interactions; coupled climate model.

1. Introduction

The climate of South Asia is dominated by the monsoon, which returns with remarkable regularity in each summer and provides the rainfall needed to sustain over 60% of the world's population. The Indian subcontinent is thus strongly dependent on the timing and amount of precipitation falling during the monsoon season (from June through September, JJAS hereafter) and is one of the most vulnerable regions of the world as far as water resources is concerned. Predicting and projecting (for the next century) the Indian Summer Monsoon (ISM) rainfall variability are, thus, both a scientific challenge and a key-societal need.

On inter-annual time scales, the ISM rainfall exhibits the multiyear (3-7 years) El-Niño-Southern-Oscillation (ENSO) frequency (Mooley and Parthasarathy 1983; Webster et al. 1998; Lau and Wang 2006). ENSO is the most dominant form of ocean-atmosphere coupled variability on interannual time scales and affects climate worldwide through atmospheric and oceanic teleconnections (e.g., Tourre and White 1995; Alexander et al. 2002; Clarke 2008; Wang 2019). The effect of ENSO on the ISM has been intensively studied for decades (Walker 1924; Sikka 1980; Keshavamurthy 1982; Webster et al. 1998; Lau and Nath 2000, 2012; Gadgil et al. 2004; Cherchi et al. 2007; Pillai and Anamalai 2012). During El Niños, the Walker circulation shifts eastward, inducing subsidence and dry conditions in the Indian sector and vice-versa during La Niñas (Walker 1924; Sikka 1980; Rasmusson and Carpenter 1983; Webster et al. 1998; Lau and Nath 2000, 2012). It is therefore extremely important to examine if the ENSO-ISM relationships are well simulated in state-of-the art climate and seasonal forecasting models (Annamalai et al. 2007; Terray et al. 2012; Sperber et al. 2013; Jourdain et al. 2013; Sabeerali et al. 2019; Krishna et al. 2019).

Though the probability of occurrence of a weak (strong) ISM during an El Niño (La Niña) is large, still ENSO can explain only about 35% the interannual variance of ISM rainfall (Krishna Kumar et al. 2006). Moreover, the ISM-ENSO relationship has considerably weakened during some periods (Torrence and Webster 1999), so that it is important to look for other sources of ISM predictability. In addition to ENSO, many studies have pointed out significant connections between ISM and the Indian Ocean (IO) Sea Surface Temperatures (SST) anomalies (Rao and Goswami 1988; Ashok et al. 2001, 2004; Gadgil et al. 2004, 2005, 2007; Krishnan et al. 2003; Terray et al. 2003, 2007; Cherchi et al. 2007; Park et al. 2010; Boschat et al. 2011; Lau and Nath 2012; Cherchi and Navarra 2013; Shukla and Huang 2016). In particular, it has been suggested that the Indian Ocean Dipole (IOD; Saji et al. 1999; Webster et al. 1999) interacts with both ENSO and ISM (Ashok et al. 2001, 2004; Drbohlav

et al. 2007; Loschnigg et al. 2003; Schott et al. 2009; Luo et al. 2010; Izumo et al. 2010; Wang 2019). Positive IOD events are associated with cool SST and shallow thermocline in the eastern Indian Ocean (IO), and warm SST and deep thermocline in its western part (Li et al. 2003; Gualdi et al. 2003; Spencer et al. 2005; Fischer et al. 2005; Schott et al. 2009). The way IOD can influence ISM remains controversial. Some authors suggest a direct influence of positive IOD events through moisture transport over the western IO or modifications of the local Hadley cell with increased ascendance over India, both factors enhancing ISM rainfall (Ashok et al. 2001, 2004; Gadgil et al. 2004; Behera et al. 2005; Ashok and Saji 2007). It has also been suggested that IOD counteracts the influence of ENSO on ISM (Ashok et al. 2001, 2004; Ashok and Saji 2007; Ummenhofer et al. 2011; Krishnaswamy et al. 2015).

More recently, more complex interactions between ISM, IOD and ENSO have been evidenced, adding even more complexity to the emerging picture. It has been suggested that a strong ISM can favor a negative IOD event by producing westerly wind anomalies over the equator IO during boreal fall and that ENSO, ISM and IOD are strongly inter-related components of the Tropospheric Biennial Oscillation (TBO) in the Tropics (Terray 1995; Meehl 1997; Meehl and Arblaster 2002, 2003; Loschnigg et al. 2003; Terray et al. 2003, 2005b; Drbohlav et al. 2007; Webster and Hoyos 2010; Li and Hsu 2017). IODs have also been suggested as a potential trigger of ENSO events (Luo et al. 2010; Izumo et al. 2010; Zhou et al. 2015; Jourdain et al. 2016; Wieners et al. 2017ab; Cai et al. 2019). It has been further discovered that the the Indian Ocean Basin (IOB) mode, associated with ENSO-related subsidence during the decaying phase of El Niños (e.g., Klein et al. 1999; Alexander et al. 2002; Xie et al. 2009, 2016; Schott et al. 2009; Wang 2019), provides an important forcing on ISM variability (Yang et al. 2007; 2010; Park et al. 2010; Bosch et al. 2011, 2012; Chowdary et al. 2017).

Because of the interactive nature of the tropical Indo-Pacific ocean-atmosphere system and the near-global patterns of ISM teleconnections summarized above, one of the best tools to simulate and predict ISM variability is a global Coupled General Circulation Model (CGCM; Wu and Kirtman 2005; Wang et al. 2005; Zhu and Shukla 2013). In order to provide reliable seasonal predictions and climate projections of ISM rainfall, it is nevertheless essential that CGCMs produce a reasonable simulation of the mean summer monsoon circulation and rainfall distribution, as well as its variability at different time scales. Unfortunately, this is still an area under rapid development, and CGCMs are still at a relatively early stage (Shukla et al., 2009). Most current CGCMS exhibit deficiencies in simulating ISM, ENSO and the IO variability (Bollasina and Ming 2013; Levine et al. 2013; Prodhomme et al. 2014, 2015; Li

and Xie 2012, 2014; Li et al. 2015, 2017ac; Ham and Kug 2014; Bellenger et al. 2014; Annamalai et al. 2017; Terray et al. 2018). So far, we have only a poor understanding of the relative roles of local ocean-atmosphere coupling (e.g. IO) and ENSO in the occurrence of extreme ISMs both in observations and coupled simulations (Gadgil et al. 2005; Saha et al. 2016; Krishna et al. 2019). In particular, the way the IOD and IOB modes influence ISM and interact with ENSO remains unclear (Wu and Kirtman 2004ab; Achuthavarier et al. 2012; Li et al. 2015, Annamalai et al. 2017), and may limit drastically ISM seasonal predictability and the accuracy of ISM projections (Sabeerali et al. 2019; Li et al. 2017ac).

Taking into account the large uncertainties in the sign and amplitude of the ENSO-IO-ISM relationships, we will document in this work, (i) the ability of state-of-the-art CGCMs to simulate the ENSO-ISM relationship and (ii) the possible role of the IO (e.g. the IOD and IOB modes) in modulating this relationship. More precisely, we will document errors in the simulation of the ENSO-ISM relationship in CMIP5 and some seasonal forecasting CGCMs and analyze a set of decoupling experiments performed with a global CGCM, the SINTEX-F2 model (Masson et al. 2012), to diagnose the possible origins of these errors. Such decoupling approach has been already successfully used to analyze the role of Indian and Atlantic oceans on ENSO (Ohba and Ueda 2007; Luo et al. 2010; Santoso et al. 2012; Ohba and Watanabe 2012; Terray et al. 2016; Kajtar et al. 2017), the impacts of SST errors on ISM (Prodhomme et al. 2014, 2015), and the IOD evolution and its forcing mechanisms in the absence of ENSO (Fischer et al. 2005; Behera et al. 2005, 2006; Yang et al. 2015; Cretat et al. 2017, 2018; Stuecker et al. 2017; Wang et al. 2016, 2019).

This paper is organized as follows. The coupled models, the sensitivity experiments and validation datasets used in this study are described in Section 2. In Section 3, we document the ISM-ENSO relationships in observations and the errors in simulating these relationships by current CGCMs. In Section 4, we analyze decoupling experiments performed with the SINTEX-F2 CGCM, in which tropical Pacific or IO SST variability is removed, in order to assess the “intrinsic” role of IO SSTs on ISM, ENSO and the ISM-ENSO relationship and to understand their potential roles on the errors in the simulation of the ISM-ENSO relationship. The final section summarizes the main results of the present work and discusses if and how these results apply to CMIP5 models.

2. Observed datasets, coupled models and sensitivity decoupling experiments

2.a Observed datasets

To study ISM variability and its teleconnection with ENSO, we have used three different observed rainfall datasets. Firstly, we considered the extensively used classical All-India-Rainfall (AIR) dataset, based on quality-controlled rain-gauge data, for the period 1870-2012 (Parthasarathy et al., 1994; Krishna Kumar et al. 1999; Bodai et al. 2020). The second rainfall dataset included in our analysis is a high-resolution (e.g. $0.25^\circ \times 0.25^\circ$) quality-controlled gridded (daily) rainfall dataset, for the period 1901-2013, as obtained from the Indian Meteorological Department (IMD; see Pai et al. 2015 for precise details). Finally, we also used the Global Precipitation Climatology Project rainfall dataset (GPCP at $1^\circ \times 1^\circ$ spatial resolution; Huffman et al. 2001), which combines measures of precipitation gauges and satellite data. GPCP is analysed for the 1979-2012 period. For both IMD and GPCP, the ISM Rainfall (ISMR) time series is defined as the average of rainfall anomalies for the land grid points in the region 5°N to 25°N and 70°E to 95°E .

The Niño-3.4 SST (monthly average of SST anomalies in the region 5°S to 5°N and 170° to 120°W) time series is chosen for the ENSO index since in observations the strongest correlations between ISMR and tropical Pacific SSTs occur over this region (not shown). This is consistent with past studies (Krishna Kumar et al. 2006; Jourdain et al. 2013). However, this practical choice implies that our study mainly focuses on canonical ENSO events rather than on El Niño Modoki events (Ashok et al. 2007). The Niño-3.4 SST time series is estimated from the Hadley Centre Sea Ice and SST dataset (HadISST1.1; Rayner et al. 2003). But similar results (not shown) are obtained with other SST datasets such the ERSST dataset (Huang et al. 2017) or the AVHRR only daily Optimum Interpolation SST version 2 (OISSTv2) dataset (Reynolds et al. 2007).

2.b Climate models

In order to give a complete overview of the capacity of current CGCMs to simulate the ENSO-ISM relationship, we first considered monthly mean outputs from Coupled Model Intercomparison Project Phase 5 (CMIP5) coupled models available at url: http://cmip-pcmdi.llnl.gov/cmip5/data_portal.html (Taylor et al. 2012). We analyzed the twentieth century simulations of 25 CMIP5 models (see Table S1 in Supplementary Materials for list of models) and for all the models we use the first ensemble member (“r1i1p1” from CMIP5 database) from each model. We also used long free runs of two state-of-the-art global CGCMs, the CFSv2 (Saha et al. 2014) and the SINTEX-F2 (Masson et al. 2012). The lengths of these control simulations are 80 and 210 years, respectively, for the CFSv2 and SINTEX-F2 CGCMs.

The CFSv2 is the CGCM adopted for operational seasonal forecasting in the US by the National Centers for Environmental Prediction (NCEP; Saha et al. 2014) and in India, in the framework of the Monsoon Mission project (Rao et al. 2019). Its atmospheric model, the Global Forecast System (GFS) is run at T126 spectral resolution (about 0.9° by 0.9°) with 64 sigma-pressure hybrid levels. Its oceanic component has a 0.25 - 0.5° horizontal resolution, 40 vertical levels and includes an ice model. The atmosphere and ocean exchange quantities such as heat and momentum fluxes every half an hour, with no flux adjustment. See Saha et al. (2014) for further details on the CFSv2 model.

The SINTEX-F2 is used by JAMSTEC (e.g. Japan) for operational seasonal forecasting (Luo et al. 2005; Doi et al. 2016). A comprehensive description of SINTEX-F2 can be found in Masson et al. (2012). The atmospheric component is ECHAM5.3 and is run at T106 spectral resolution (about 1.125° by 1.125°) with 31 hybrid sigma-pressure levels (Roeckner et al. 2003). The oceanic component is NEMO (Madec 2008), using the ORCA05 horizontal resolution (0.5°), 31 unevenly spaced vertical levels and including the LIM2 ice model (Timmermann et al. 2005). The coupling information, without any flux corrections, is exchanged every 2 h using the Ocean-Atmosphere-Sea Ice-Soil coupler (Valcke 2006). The performance of the SINTEX-F2 model in simulating the mean state and interannual variability in the Indo-Pacific areas has been assessed many times and is not repeated here (Masson et al. 2012; Terray et al. 2012, 2016, 2018; Prodhomme et al. 2014, 2015; Cretat et al. 2017, 2018).

Note, finally, that the SINTEX-F2 and CFSv2 configurations used here employ fixed CO_2 concentrations corresponding to present day conditions. This is consistent with the use of recent observations (e.g. mostly 1979-2012) for validation of model outputs.

In all simulations, we characterize the ISM by the JJAS average precipitation over India (5° - 25°N and 70° - 95°E , land only; ISMR index hereafter) and ENSO by the Niño-3.4 box-average SST as in observations.

2.c Partial decoupling experiments

In addition to the 210-year control run described above (named CTRL hereafter), we perform three partial decoupling experiments (named FTPC, FTIC and FSEIC hereafter), where the model SSTs in the tropical Pacific, Indian oceans and SEIO region are, respectively, nudged to a daily SST climatology obtained from CTRL (see Table 1 for details and definition of the acronyms used to design the nudged experiments), as described in Luo et al. (2005) and Appendix. The damping constant used is $-2400 \text{ W m}^{-2} \text{ K}^{-1}$, which corresponds

to the 1-day relaxation time for temperature in a 50-m ocean layer. In these experiments there are no significant changes in SST mean state and seasonal cycle in the nudged regions, but also in the whole Tropics compared to CTRL (see Figs. 1b-d and 2), but, SST variability is suppressed in the nudged region (not shown; see Terray et al. 2016 and Cretat et al. 2017 for illustration). The FSEIC experiment is designed to assess the role of the SST SEIO variability, and by extension of the IOD (as the SEIO region almost matches the eastern pole of the traditional IOD index in observations). Furthermore, despite the SST SEIO bias is modest in the annual mean (Fig. 1a), this region is affected by severe seasonally varying SST mean and variability biases in the SINTEX model (Fig. 2; Fischer et al. 2005; Terray et al. 2012; Prodhomme et al. 2014; Cretat et al. 2017). The CGCM simulates a too shallower thermocline in the eastern Indian Ocean during boreal summer and fall. The thermocline-surface coupling is thus amplified in the annual cycle with deeper and cooler water easily upwelled at the surface, cooling drastically the SST mean and enhancing the SST variability in the SEIO during boreal summer and fall (Fig. 2). In addition, the SEIO SST is affected by a strong warm mean bias and also a too strong SST variability during late boreal winter in CTRL (Fig. 2). The FSEIC experiment will therefore be useful to understand the specific role of this amplified SST variability in the SEIO during these two critical seasons on the simulated ENSO, ISM and their relationships.

Finally, in order to discuss the remote or local origins of these SST errors in the SEIO in Section 5, an additional partial decoupling experiment (named FTPC-obs hereafter) will be considered. This run is similar to the FTPC experiment, excepted for the use of a daily climatology computed from the OISSTv2 dataset for the 1982-2010 period (Reynolds et al. 2007) in the nudging procedure (Table 1). In this FTPC-obs run, the large feedback value applied removes the SST mean biases (in CTRL) with respect to the observed SST climatology, in addition of suppressing the SST variability in the restoring tropical Pacific domain (Fig. 1e).

Table 1 summarizes the specifications of the different sensitivity experiments used here and the different nudging domains are displayed in Fig.1b-d. Finally, in the analyses described in Sections 3, 4 and 5, the first 10 years of all simulations have been excluded due to the spin-up of the coupled model.

3. ISM-ENSO relationships in observations and CGCMs

We first document the amplitude and timing of the relationship between ENSO and ISM in

observations in order to provide a basis for a fair assessment of the performance of current CGCMs with respect to this metric in the next subsection.

3.a Observed ISM-ENSO relationships

In order to illustrate this relationship, we computed the lead-lag correlations between the different ISMR time series and the Niño-3.4 SST bimonthly time series in a three years window from the beginning of year -1 to the end of year +1, the year 0 referring to the year of the ISM season (Fig. 3a-b). Correlation coefficients have been estimated with and without detrending of the different rainfall and SST time series in order to assess the robustness of the results with respect to anthropogenic related trends and nonstationarity of the time series. Detrending has been performed with locally weighted regression, a non-parametric method for fitting a smoothed regression curve to data through local smoothing (Cleveland and Devlin 1988). As results are similar, we only show the results from detrended data here.

Consistent with the TBO pattern, involving ENSO and ISM (Yasunari 1990; Meehl 1997; Meehl and Arblaster 2002; Loschnigg et al. 2003; Terray et al. 2003, 2005b; Webster and Hoyos 2010), two distant correlation peaks of opposite signs are noted (Fig. 3a-b). Positive correlations are evident one year before the monsoon for most ISMR indices and time periods. These significant positive correlations preceding ISM have largely amplified during recent decades, e.g. after the 1976/77 climate shift and have been explained by a delayed ENSO effect on the ISM, mediated by the IOB warming, which follows the strong El Niño events, such as the 1982-83 and 1997-98 events (Yang et al. 2007, 2010; Park et al. 2010; Boschat et al. 2011, 2012). The correlations switch sign around April-May (AM) and become again statistically significant only in June-July (JJ) of year 0 (Webster and Yang 1992; Webster et al. 1998). These negative correlations between Niño-3.4 SSTs and ISMR peak during boreal fall and fade away progressively after, e.g. during the peaking and decaying phases of El Niño (Fig. 3a-b). The significant negative correlation between ISMR and Niño-3.4 SSTs during boreal summer of year 0 implies that warmer (cooler) SSTs over these regions will suppress (enhance) ISM rainfall consistent with the studies summarized in the introduction. This synchronous effect can be termed the “direct” ENSO effect by opposition to the “indirect” effect mediated by the IOB warming induced by ENSO (Wu et al. 2012).

Fig. 3a-b also demonstrates that the synchronous correlation between ISM and ENSO is decreasing for more recent (and shorter) time periods. Interestingly, the lead correlations between ENSO of year -1 and ISM follow an opposite evolution. The decreasing synchronous correlation has lead to the suggestion that the ISM-ENSO relationship has weakened during

recent decades for reasons which are still a matter of debate (Krishna Kumar et al. 1999, 2006; Torrence and Webster 1999; Gershunov et al. 2001; Ashok et al. 2001, 2004, 2007; Kinter et al. 2002; Annamalai et al. 2007; Kucharski et al. 2007, 2008; Chen et al. 2010; Boschat et al. 2012; Li and Ting 2015; Srivastava et al. 2015; Cash et al. 2017; Yun and Timmermann 2018; Feba et al. 2019; Bodai et al. 2020).

3.b Simulated ISM-ENSO relationships

We first focus on the capacity of the SINTEX-F2 and CFSv2 coupled models to simulate the ISM-ENSO relationship (Fig. 4a). The two CGCMs are able to reproduce the synchronous negative correlation between ISM and ENSO, though with varying amplitude (Fig. 4.a). However, before ISM, the two CGCMs show large discrepancies from observations with negative and significant correlations during an extended period of several months before ISM. In the CFSv2 model, the lead-lag correlations suggest that ISM is linked to ENSO *before ISM rather than during and after ISM* since the maximum negative correlation occurring at lag 0, e.g. JJ of year 0. Moreover, after ISM, the negative correlation quickly fades away in disagreement with observations. The SINTEX-F2 performs slightly better, but shares the same deficiency during the pre-onset period.

We next examined the lead-lag correlations between the Niño-3.4 SST and ISMR in CMIP5 CGCMs (Fig. 5a). Here, the correlation coefficients are computed from the first member of each model's ensemble of historical runs and for the period 1950-2000. ISM and its relationships to ENSO in CMIP5 models have already been investigated in many studies (Sperber et al. 2013; Terray et al. 2012); Jourdain et al. 2013; Ramu et al. 2018), but most of them focus on the synchronous relationship (e.g. during boreal summer) between the two phenomena. Here we examine the lead-lag relationships between the two phenomena in more details following the same framework as used above for observations, the SINTEX-F2 and CFSv2 models, complementing the results of Jourdain et al. (2013).

Many CMIP5 CGCMs are able to reproduce the synchronous negative correlation between ISM and ENSO, although in many models the amplitude of this correlation is erroneous and the diversity (e.g. spread) is large between the CGCMs (Figure 5a). However, a striking feature is that almost all of the CMIP5 CGCMs fail to capture the observed lead-lag relationships between ENSO and ISM. In particular, most CGCMs show erroneous large negative correlations before ISM, which are completely absent in observations, and the observed TBO pattern with positive correlations preceding the ISM by nearly one year is lacking in all CMIP5 CGCMs. In a similar fashion, the simulated correlations are much

weaker than observed after the boreal summer of year 0.

In other words, current CGCMs show large deficiencies in recovering the observed lead-lag relationships between ISM and ENSO, which is of paramount importance for seasonal forecasting (Gadgil et al. 2005) or climate projections of ISM rainfall (Li et al. 2017ac). It is therefore necessary to go a step further in the model validation to analyze more thoroughly the reasons of this deficiency in current CGCMs, which is the goal of the next sections.

3.c Simulated ENSO seasonal phase-locking

Though considerable improvements in the simulation of ENSO have been made during the past decades, current CGCMs still need to be improved with regard to realistically representing ENSO (Bellenger et al. 2014). As an illustration, the tendency to produce a double intertropical convergence zone in the Pacific basin, a poor representation of the SST annual cycle and mean pattern in the tropical Pacific, and a substantial underestimation of ENSO variability are recurrent biases shared by many past and present CGCMs (AchutaRao and Sperber 2002, 2006; Li and Xie 2012; 2014; Bellenger et al. 2014). Thus, a biased representation of ENSO in the tropical Pacific itself can be a primary plausible reason for an improper simulation of the ISM-ENSO relationship in current CGCMs (Jourdain et al. 2013). However, Indian and Atlantic SSTs can also matter as they have an overall damping effect on ENSO and modulate the length of the ENSO events (Dommenget et al. 2006; Terray et al. 2016).

The phase locking of ENSO events to the annual cycle, with a tendency to peak at the end of the calendar year, the amplitude and length of El Niño events (e.g. ENSO periodicities) are among the most distinctive characteristics of ENSO (Rasmusson and Carpenter 1983; Clarke 2008; Ham and Kug 2014; Li and Hsu 2017). Obviously, the incorrect annual phase-locking of ENSO's variability is a plausible candidate for explaining the current failure of state-of-the-art CGCMs in the simulation of the ISM-ENSO lead-lag relationships, since most coupled models do simulate a boreal summer monsoon over India (Figs. 4d and 5d). In Figures 4b and 5b, we show the monthly standard deviations of the Niño-3.4 SST anomalies from observations, the SINTEX-F2, CFSv2 and CMIP5 CGCMs, respectively. Observed ENSO variability typically peaks in boreal winter and diminishes in boreal spring with relatively modest variability in boreal summer and early fall (Fig. 4b), which is related to the fact that El Niño's onset frequently occurs in boreal spring or early boreal summer (Clarke 2008).

It is apparent that both the SINTEX-F2 and CFSv2 models have a preference for relatively high SST variability in the Niño-3.4 region during boreal winter, as observed (Fig. 4b).

However, the monthly Niño-3.4 SST standard deviations in these models are higher than observed during boreal spring suggesting that ENSO onset is early than observed or that ENSO decay is slower than observed in the CGCMs. This bias is consistent with the lead-lag ISM-ENSO relationships simulated in the two models, especially the unrealistic negative correlations between ISM and the Niño-3.4 SST preceding the ISM onset (Fig. 4b). This is further confirmed by a lead-lag correlation analysis of SSTs with the ISMR index in the SINTEX-F2 model (see Fig. S1a-f or Figures 3 and 5 of Bosch et al. (2012) for similar analysis on observations). Also consistent with these erroneous negative correlations, the ISM rainfall monthly standard deviations are also exaggerated at the beginning of ISM in the simulations (Fig. 4c).

On the other hand, many CMIP5 models show a different seasonal Niño-3.4 SST evolution, with the peak of canonical El Niños occurring at any season (Fig. 5b; Ham and Kug 2014; Taschetto et al. 2014) and only a few models have Niño-3.4 SST variability above observations during boreal winter (Fig. 5b). This can be related to many factors, especially spatial shift of simulated SST variability over the equatorial Pacific often associated with the cold tongue bias (Collins et al. 2010; Li and Xie 2014; Swapna et al. 2015). However, most of them also produce a too large and erroneous ENSO variability during boreal spring as the SINTEX-F2 and CFSv2 models (Figs. 4b and 5b). Consistent with this deficiency and the erroneous negative correlations before ISM (Fig. 5a), the simulated ISM rainfall monthly standard deviations are again exaggerated at the beginning of ISM in most CMIP5 models (Fig. 5c). This exaggerated simulated ENSO variability during boreal spring and early summer can be due to (i) ENSO onsets occurring earlier in the CGCMs, (ii) ENSO events lasting longer with an extended maturing phase compared to observations, or both.

While SST mean biases, ENSO pattern or position of peak and deficient ENSO teleconnections may also modulate ISM-ENSO relationships in CGCMs (Jourdain et al. 2013), we will show in the next section that length and seasonal phase-locking of ENSO events are key-factors for a realistic simulation of the lead-lag ISM-ENSO relationships.

4. Indian Ocean impacts on the ENSO-ISM relationship in the SINTEX-F2 CGCM

To disentangle the role of IO SST variability in shaping the ISM-ENSO relationships, we now analyzed decoupling experiments performed with SINTEX-F2 (see Section 2c).

4.a Intrinsic ISM teleconnections

We first investigate the possible “intrinsic” role of SST anomalies outside of the tropical Pacific on the ISM, as an important factor in shaping the ENSO-ISM relationship. The analysis is done with the help of the FTPC simulation, where ENSO is removed. By contrast, in the next subsection, we will investigate the possible role of IO SST anomalies on ENSO itself, as a second factor in shaping the simulated ENSO-ISM relationship with the help of the other sensitivity experiments in which the tropical IO SST variability, or parts of it, is suppressed.

Figure 6.a-d displays the regressions of the JJ and August-September (AS) 850-hPa wind and rainfall fields onto the ISMR index for CTRL and FTPC. As expected, Fig. 6.a-d show enhanced rainfall over India and the neighboring oceanic regions, as well as a strengthening of both the monsoon low-level winds over the Arabian Sea and the Somali jet along the African coast. Next, ISM rainfall anomalies are very sensitive to the perturbation of the Walker circulation that is characteristic of La Niña/El Niño episodes in CTRL (Fig. 6.a-b). Positive rainfall anomalies develop over the maritime continent and neighboring ocean areas and a negative IOD like rainfall pattern emerged over the equatorial IO during AS of strong ISMs and La Niña episodes, consistent with previous works (Webster et al. 1998; Lau and Nath 2000, 2003, 2012; Cretat et al. 2017).

By contrast, in FTPC, the atmospheric response associated with the strong/weak ISMs is mostly confined northward of 10°N and is characterized by an anomalous rainfall pattern opposing India and the northwest Pacific region (Fig. 6c-d; Terray et al. 2005a; Wang 2006; Gu et al. 2010; Kosaka et al. 2013; Cretat et al. 2017). Interestingly, ISMR rainfall standard deviations are only slightly reduced (at most of 0.2 mm/day, see Fig. 8c) in FTPC. This result may seem contradictory with the expectation that ENSO is the main driver for ISM interannual variability, but is consistent with the large internal variability associated with ISM and the fact that ISM is also an active player in tropical climate (Yasunari 1999; Kirtman and Shukla 2000). Further, boreal summer rainfall and wind anomalies are very weak outside this north Indo-Pacific region, especially over the equatorial IO.

We now examine the extent to which SST forcing outside the tropical Pacific may explain ISM rainfall variability in the absence of ENSO. This is done through a lead-lag correlation analysis between the ISMR index and bi-monthly SST and 200-hPa velocity potential anomalies in the CTRL and FTPC experiments (Figs. S1 and 7). Correlations between ISMR and SSTs in CTRL confirm the existence of a significant statistical association between ISM, ENSO and IOD (Fig. S1a-f), as discussed in the Introduction. Some significant correlations are also seen in the extratropical Pacific and the tropical Atlantic during boreal summer and

winter (Fig. S1c-f), which are also consistent with well-known ENSO teleconnections (Wang 2019). On the other hand, correlations between ISMR and SSTs are strikingly different in FTFC (Fig. 7a-f). They are weak before, during and after ISM, except for a significant cooling (warming) of the Arabian Sea (the south of the bay of Bengal) during boreal summer (Fig. 7a-f). This local response is fully consistent with a “slave ocean scenario” in which the SST is mainly controlled by evaporative cooling and local upwelling associated with the strengthening of the monsoon low-level winds and the sea-saw between ISM and the northwest Pacific monsoon discussed above (see Fig. 6c-d). Moreover, simulated ISM variability is not significantly associated with SST anomalies or modulations of the Walker cell over the equatorial IO during boreal summer and fall (Fig. 7c-e and i-k) despite the fact that IODs do exist in the absence of ENSO in FTFC (Fig. 2b; Cretat et al. 2017, 2018). These results invalidate the hypothesis that the direct impact of IOD on ISM may induce a significant modulation of the ENSO-ISM relationship in SINTEX-F2.

On the other hand, the results in CTRL (Fig. S1) are fully consistent with a scenario in which ENSO, ISM and IOD are strongly inter-related components of the TBO in the Tropics (Meehl and Arblaster 2002, 2003; Drbohlav et al. 2007; Webster and Hoyos 2010) since a strong ISM is significantly correlated with La Niña and a negative IOD in CTRL (Fig. 6a-b and S1). However, the FTFC experiment demonstrates that this ENSO-ISM-IOD coupling is mainly due to the ENSO forcing on both ISM and the equatorial IO separately, and not to a direct association between ISM and the equatorial IO, at least in this CGCM.

Furthermore, the 200-hPa velocity potential anomalous patterns associated with ISMR variability confirm the hypothesis that ISM is an active player for the whole tropical circulation in the absence of ENSO. The only physically consistent anomalous 200-hPa velocity potential pattern emerging in Fig. 7g-l is the strong upper-level divergence flow associated with ISM itself and the induced significant strengthening of the subtropical anticyclones over the Pacific and South Atlantic (Fig. 7i-j). Thus, the upper-level circulation anomalies during boreal summer in FTFC are dominated by an enhancement of the zonal monsoon cyclone-subtropical anticyclone circulation driven by the east-west differential heating (Rodwell and Hoskins 2001; Chen 2003). On the other hand, in CTRL, the 200-hPa velocity potential correlation pattern (Fig. S1g-l) has a more large-scale structure and is tightly and significantly linked to ENSO evolution (Fig. S1a-f), as expected (Webster et al. 1998).

In summary, the results of this section strongly suggest that direct (e.g. when ENSO is removed) effects of interannual SST anomalies outside of the tropical Pacific on ISM are

weak and do not play a direct role in shaping the ENSO-ISM relationship in the SINTEX-F2 model.

4.b Indian Ocean impacts on ENSO

However, the tropical IO can also influence the ENSO-ISM relationship by directly modulating ENSO in the tropical Pacific itself. Many studies have also highlighted the strong impact of the IOB in accelerating the El Niño to La Niña transition in the tropical Pacific (Kug and Kang 2006; Dommenges et al. 2006; Ohba and Ueda 2007; Jansen et al. 2009; Okumura et al. 2011; Ohba and Watanabe 2012; Kug and Ham 2012; Santoso et al. 2012; Terray et al. 2016; Xie et al. 2009, 2016; Kajtar et al. 2017). Several authors suggested that positive IOBs generate easterly wind anomalies over the western Pacific during boreal winter and spring as an atmospheric Kelvin wave response to the local diabatic warming (Annamalai et al. 2005; Terao and Kubota 2005; Kug and Kang 2006). Watanabe and Jin (2002) also argued that a positive IOB strengthens an anomalous low-level NorthWest Pacific Anticyclone centered on the Philippine Sea (NWPAC, also referred to as Philippine Sea anticyclone or western North Pacific subtropical high in the literature; see Wang et al. 2000) during the mature-decayed phase of El Niño. Collectively, these atmospheric anomalies may fasten the transition from El Niño to La Niña since the associated zonal wind stress anomalies over the western Pacific force upwelling oceanic Kelvin waves that propagates eastward along the Equator and favor the transition to the La Niña phase (Kug and Kang 2006; Ohba and Ueda 2007; Ohba and Watanabe 2012; Kug and Ham 2012; Wang 2019). Some recent studies suggest, on the other hand, that the major forcing for the NWPAC during boreal winter is from the central Pacific, as rainfall anomalies and associated diabatic warming over the IO are very modest during this season and, thus, cannot trigger an atmospheric Kelvin wave intruding into the western Pacific (Chen et al. 2016; Wu et al. 2017ab; Li and Hsu 2017; Li et al. 2017b). Luo et al. (2010) and Izumo et al. (2010) also found that IOD has highly significant impacts on both ENSO variability and predictability.

Our decoupling experiments allow to reinvestigate the significance of the IO feedback during boreal winter and spring in a consistent modeling framework, and may challenge the view that this IO negative feedback is weak during boreal winter (Li et al. 2017b). Moreover, what may be the impact of IO variability on the ENSO-ISM relationships despite the modest role of IOD on ISM suggested above?

To answer this question, Figure 8a-b displays the Niño-3.4 SST-ISM lead-lag correlations and the monthly Niño-3.4 SST standard deviations in the FTIC and FSEIC

experiments in which IO or SEIO SST variability is removed (see Table 1 and Section 2c). The negative Niño-3.4 SST-ISM correlations before the ISM onset and ISMR standard deviations during (early) boreal summer are substantially amplified in FTIC, while the ISMR seasonal cycle remains the same (Fig. 8a, c-d). In other words, FTIC showed prominent negative correlations with the Niño-3.4 SSTs *before rather than synchronous and after* the ISM. These errors, already present in CTRL, are thus significantly amplified in FTIC. By contrast, the simulated ISM and ENSO relationships in FSEIC closely resemble the observed ones (Fig. 8a). FSEIC is able to recover the slow change of sign of the ISM-ENSO correlations from positive to negative from year -1 to year 0 as observed. The differences between the simulated and observed correlations for the different lags have been tested for statistical significance with a Fisher Z transform approach (see Morrison 1990; pp 102-106) and FSEIC is the only simulation, which does not show any statistical difference with observations at the 95% confidence level for any lags. Interestingly, this success is not related to changes in the SST mean state (Figs. 1d and 2a) or ISMR seasonal cycle (Fig. 8d). Evidences will be presented in this section to demonstrate that these large improvements are related to changes in the characteristics of the model's El Niño during its decaying phase in FSEIC.

Consistent with a strong damping of ENSO variability by IO variability, the Niño-3.4 SST standard deviations increase significantly in FTIC (Fig. 8b). This increase is more prominent during boreal spring and summer, which correspond to ENSO transitions. This suggests that ENSO is less phase-locked to the annual cycle and that the length of ENSO events has increased in FTIC. On the other hand, the Niño-3.4 SST variability is decreased in FSEIC compared to both CTRL and FTIC. Interestingly, the Niño-3.4 SST monthly standard deviations, as simulated by FSEIC, now match the observed Niño-3.4 SST standard deviations during ENSO transitions (e.g. boreal spring). This suggests that ENSO events start later or last shorter in FSEIC. In order to quantify more rigorously these differences between the simulations, power spectra of the simulated Niño-3.4 SST time series are shown in Figure 9. Both FTIC and FSEIC spectra are strikingly different from CTRL spectrum, e.g. ENSO is predominantly biennial or quasi-biennial in FSEIC while it lasts much longer in FTIC than in CTRL and these results are statistically significant at the 95% confidence level (Fig. 9). These important differences not only confirm that IO SSTs interact significantly with ENSO in the SINTEX-F2 model, but also suggest that the spatial and temporal details of IO SST variability play also a substantial role in the damping (or enhancement) and the length of the simulated ENSO.

We first focus on the synchronous ISM-ENSO teleconnection during boreal summer. The rainfall and 850-hPa regressions onto the ISMR index in FTIC have spatial patterns similar to those in CTRL during JJ and AS (Fig. 6e-f). This demonstrates again that ENSO forcing is critical and that local ocean-atmosphere coupling is only a secondary factor for the generation of these anomalous patterns. However, consistent with a stronger (and partly erroneous) ENSO teleconnection during early summer (Fig. 8a,c), the rainfall and 850-hPa anomalies have greater amplitude almost everywhere in the Indo-Pacific region during JJ than AS in FTIC (Fig. 6e-f). The monsoon flux over the western IO is further increased during the whole ISM in FTIC compared to CTRL, resulting in enhanced rainfall over the Arabian Sea and western India (Fig. 6e-f). Interestingly, a negative IOD like rainfall pattern also emerges along the Equator in FTIC despite the absence of local coupling, demonstrating again the strong ENSO forcing on the regional rainfall pattern (Fig. 6e, f). In FSEIC, the 850-hPa wind and rainfall regressions onto the ISMR index show that the ISM-ENSO teleconnection gradually increases from JJ to AS in contrast to FTIC (Figs. 6g-h).

However, the interactions between the Indian and Pacific oceans need not to be restricted to the boreal summer, and may concern other seasons as well, and still be important for shaping the ENSO-ISM relationship. Indeed, the negative lagged correlations of ISM with the Niño-34 SSTs during boreal winter and spring preceding ISM are very different, while the lead correlations between ISM and the following Niño-34 SST anomalies are very similar among the simulations (Fig. 8a), suggesting that the IOB may play a prominent role in the ENSO damping and explain the relative success of FSEIC compared to both CTRL and FTIC.

In order to test the hypothesis that the IOB produces a direct forcing on ENSO itself in the simulations, Figs. 10 to 12 display lagged regressions of tropical Indo-Pacific SST, rainfall, 850-hPa wind and depth of 20°C isotherm anomalies during year +1 onto the December-January (DJ) Niño-3.4 SST index in the different simulations. Here, numerals such as 0 and +1 denote the ENSO developing (0) and decay (+1) years, respectively. Lagged regressions of 850-hPa stream function, 850- and 200-hPa velocity potential anomalies during February-March (FM) of year +1 onto DJ Niño-3.4 SST index are also displayed in Fig 13 in order to diagnose physical processes responsible of the differences in ENSO damping between the simulations.

First, the results confirm the robustness of the link between the decaying phase of El Niño events and the IOB in CTRL and FSEIC in which ocean-atmosphere coupling is (partly) active in the IO (Figs. 10a and 10c). As expected, the SST regression patterns over the tropical Pacific during FM(+1) show enhanced warming over the central and eastern Pacific

and a well-developed cold horseshoe signature in the extra-tropical Pacific in all experiments. However, the Pacific SST anomalies are more confined meridionally in the FSEIC experiment during FM(+1) and AM(+1) (Fig. 10c). The IO warming is basin-wide and uniform in CTRL and absent by design in FTIC (Fig. 10a-b). On the other hand, decoupling the SEIO enhances the warming in the other IO areas, especially over the western IO, and leads to a substantial anomalous SST equatorial gradient in the IO during FM(+1) (Fig. 10c). The modulation of the Walker circulation during El Niño induces local atmospheric subsidence (Fig. 13), which reduces cloud cover and forces near surface wind anomalies (Fig. 11) and surface heat fluxes over the IO, and, thus, initiates and sustains the basin-wide IOB warming in CTRL and FSEIC (Klein et al. 1999; Alexander et al. 2002; Schott et al. 2009).

Next, Fig. 10 illustrates that the Pacific SST anomalies during boreal spring and summer of the decaying phase of ENSO are different in the three simulations. First, the El Niño related warm anomalies persist up to the boreal summer of year +1 in FTIC, but have disappeared by the end of boreal spring in FSEIC, while CTRL exhibits an intermediate evolution of tropical Pacific SST anomalies between these two extreme scenarios. These results are consistent with the different seasonal phase locking of Niño-3.4 SST variability in the simulations (Fig. 8b). Cold equatorial Pacific SST anomalies emerge during boreal summer in FSEIC, signaling the beginning of a La Niña episode. Because of the slow response of the IO to ENSO forcing, the IOB persists until the following boreal summer in both CTRL and FSEIC (Figs. 10a, c). Surprisingly, IOB warming is more intense in FSEIC than in CTRL despite of the quick demise of the El Niño SST pattern in FSEIC.

In summary, these results first demonstrate that the IOB has a considerable impact on the anomalous climate during the decaying phase of ENSO in SINTEX-F2 (Figs. 10 to 12), consistent with previous studies (Kug and Kang 2006; Ohba and Ueda 2007; Ohba and Watanabe 2012; Terray et al. 2016; Cai et al. 2019; Wang 2019). However, the significant differences between FSEIC and CTRL highlight that the details of the IOB warming, especially the SST differences between the western IO and SEIO during late boreal winter, do also matter a lot, which is an important result of the present study.

In order to provide an explanation, we focus on the atmospheric circulation during FM(+1) (Fig. 13), when the differences in IO SST anomalies between the simulations are particularly well developed (Fig. 10 first row of panels). During the peak of El Niño, all the simulations show an enhanced convective activity over the central equatorial Pacific and reduced rainfall over the Maritime Continent (not shown) and such anomalous diabatic heating pattern is still seen during FM(+1), despite that Maritime Continent rainfall starts already to recover during

this season (Fig. 11 first row of panels). The associated 850- and 200-hPa velocity potential anomalies reveal that the Walker circulation shifts eastward in response to the diabatic warming (cooling) due to the enhanced (reduced) convection over the central Pacific (Maritime Continent). The 850-hPa stream function anomalies reveal a quadrupole structure straddling the Equator and asymmetric about it, which can be interpreted as a direct Rossby wave response to this anomalous convective pattern in all experiments (Fig. 13a,e,i). This four-cell structure plays a fundamental role in the maintenance of the rainfall and anomalous low-level circulation (Fig. 11, first row of panels), and is largely contributed by the tropical Pacific SST anomalies, which are very similar in the different simulations.

Focusing now on the IO and west Pacific, important differences in both the position and strength of the NWPA and its southern hemisphere counterpart exist between the simulations (Fig. 13a,e,i), which can directly be related to the different SST anomalies in the IO (Fig. 10 first row of panels). First, in both CTRL and FSEIC, in which IOB warming is present, these anticyclones are shifted eastward and the NWPA becomes stronger than its southern hemisphere counterpart. Second, these shifted anticyclones are further considerably strengthened in FSEIC compared to CTRL in response to a well-developed anomalous east-west circulation over the equatorial IO due to the enhanced SST zonal gradient in this run (Fig. 13j-k). Such an anomalous Walker cell over the IO is obviously absent in CTRL (Fig. 13b-c) in which the IOB warming is basin-wide and uniform (Fig. 10a). Moreover, this zonal dipole pattern in 850- and 200-hPa velocity potential anomalies in FSEIC, with anomalous ascending (descending) motion in the western (eastern) IO, is exactly similar to the observed pattern (see Fig. 5 of Li et al. 2017b for example).

Such modulation of the Walker circulation over the IO seems to be the key-factor to explain the strength of the IO negative feedback on ENSO during boreal winter in FSEIC as positive rainfall anomalies are restricted to a small region in western IO and are seen in all the runs, including FTIC in which IOB is absent (Fig. 11 first row panel). It is therefore unlikely that such restricted rainfall anomaly is associated with a well-defined basin-wide diabatic heating anomaly, which may cause an atmospheric Kelvin wave response over the Western Pacific, consistent with the view of Chen et al. (2016) or Li et al. (2017b). On the other hand, the modulation of the Walker circulation over the IO induces more upper level convergence over the Maritime Continent and western Pacific in FSEIC (Fig. 13k), which strengthens considerably the NWPA and its southern counterpart (Fig. 13i), and the associated easterly wind anomalies over the western Pacific (Fig. 13l).

Thus, our results highlight that the IOB warming, but also the existence of an anomalous

SST gradient over the equatorial IO during boreal winter, are critical for the strength/position of the NWPA, the generation of the associated anomalous easterlies over the western equatorial Pacific and, finally, the turnabout of ENSO phases in our CGCM. As the equatorial easterlies over the western equatorial Pacific are weaker in FTIC compared to CTRL and much weaker than those in FSEIC (Fig. 13d,h,i), they may consequently have only a modest influence on the Pacific SSTs one or two seasons later (Fig. 10b).

This working hypothesis, that the IOB warming and its spatial structure play a fundamental role in hastening the ENSO transition through the generation of upwelling oceanic Kelvin waves in both CTRL and FSEIC, is further supported by the regressions of the 20°C isotherm depth (e.g. a proxy for the thermocline depth) anomalies during year +1 (Fig. 12). The slow ocean dynamic adjustment in the tropical Pacific is different among the simulations. The negative heat content anomalies (e.g. a shallower thermocline), which appear over the western Pacific during the peak of El Niño, have a faster eastward propagation along the equatorial Pacific in CTRL and FSEIC (Fig. 12a,c). This eastward propagation is very gradual in CTRL (Fig. 12a), but somewhat abrupt, from AM to JJ of year +1, in FSEIC (Fig. 12c). Moreover, FSEIC shows shallower 20°C isotherm anomalies than CTRL along the equatorial Pacific (Fig. 12a,c). The enhanced zonal wind stress associated with the stronger easterly wind anomalies over the western Pacific in FSEIC induces an enhanced vertical displacement of the equatorial thermocline via Ekman pumping and the upwelling Kelvin wave response is stronger in FSEIC. The arrival of these eastward Kelvin waves into the central equatorial Pacific erodes the local surface warming (Fig. 10c). Consequently, lagging two to four months behind the remote easterly wind anomalies over the western Pacific, cold SST anomalies emerged quickly and expand westward over the central and eastern equatorial Pacific during boreal summer of year +1 in FSEIC. Such ENSO transition is delayed in CTRL (Fig. 10a) in agreement with the more modest NWPA and associated anomalous easterlies over the western equatorial Pacific during FM(+1) seen in this run.

Consistent with the reversal of the equatorial anomalous SST gradient in the Pacific, anomalous easterlies gradually emerge over the central Pacific during boreal summer of year +1 in FSEIC (Fig. 11c). On the other hand, the easterly wind anomalies over the western Pacific, seen during FM(+1) in FTIC, disappear quickly during AM(+1) (Fig. 11b). As a consequence, both the El Niño-related thermocline and SST anomalies persist and we observe a revival of the El Niño-related circulation and rainfall anomalous patterns during boreal summer of year (+1) in FTIC. Finally, the evolution is again intermediate between these two extremes in CTRL (Fig. 11a).

In agreement with these different El Niño evolutions in the simulations, we note that ISM is again highly deficient during boreal summer of the decaying phase of El Niño in FTIC, weak during JJ only in CTRL and, finally, normal or strong in FSEIC (Fig. 11 third and fourth rows). These assertions are further verified by computing regressions of boreal summer 200-hPa velocity potential anomalies onto the Niño-3.4 SST time series of the preceding boreal winter (Fig. 14). During El Niño decaying year, La Niña (El Niño) conditions prevail with a significantly strengthening (reduction) of the Walker circulation in the Indo-Pacific region in FSEIC (FTIC). Furthermore, strong (weak) upper level divergence is seen over the Indian region in FSEIC (FTIC) consistent with enhanced (reduced) diabatic heating associated with the ISM rainfall anomalies during boreal summer (Figs 11b-c third and fourth rows). Again, CTRL exhibits intermediate conditions between these two extremes with upper level convergence (e.g. subsidence) over India during JJ, but rather normal conditions in AS (Fig. 14a-b). These results demonstrate that the success to capture the seasonal evolution of the correlations between Niño-3.4 SSTs and ISMR in FSEIC (Fig. 8a) is plausibly related to the ability of this particular configuration to simulate correctly the space-time evolution of the tropical Pacific SSTs during the decaying phase of El Niño. In both CTRL and FSEIC, IOB is well developed during boreal summer of year +1 (Fig. 10a, c), but a weak (strong) ISM is simulated in CTRL (FSEIC) demonstrating that the remote ENSO forcing is still dominant in explaining the ISM response during the decaying year of El Niño. This may be understood by the fact that IOB SST anomalies are basin-wide, but of reduced amplitude during boreal summer of year +1, so that they are a significant factor for ISM variability if, and only if, tropical Pacific SST and circulation anomalies are rather weak at this stage (Figs. 10 and 11).

5. Summary and Discussion

5.a Summary

The present work examines the ability of current CGCMs in simulating the ISM-ENSO relationships. Consistent with previous studies (Terray et al. 2012; Jourdain et al. 2013; Sabeerali et al. 2019), we found that CGCMs used for climate projections or dynamical seasonal forecasting still exhibit significant errors with respect to this metric. Simulated ISM-ENSO correlations are already significant and negative several months before the ISM onset contrary to what is observed..The origins of these common errors in the simulation of the ISM-ENSO relationship are investigated based on several decoupling experiments performed

with the SINTEX-F2 CGCM.

First, a sensitivity experiment in which ENSO variability is removed (e.g. FTFC) demonstrates that relationships between ISM and SST variability outside the tropical Pacific are weak at interannual time scales in the absence of ENSO. As IODs still exist with exaggerated amplitude in such decoupling experiment in which ENSO is removed (Fig. 2b, see also Cretat et al. 2017, 2018), this suggests that IOD impact on ISM is not directly responsible of the modulated ISM-ENSO relationship in this CGCM.

On the other hand, two others decoupling experiments in which IO SST variability is fully removed (e.g. FTIC) or only in the SEIO (e.g. FSEIC) show a large spread in simulated ENSO length and decay pace. ENSO becomes predominantly quasi-biennial in FSEIC while ENSO lasts much longer in FTIC compared to CTRL. In FSEIC, cold SST and easterly wind anomalies emerge quickly in the central equatorial Pacific during boreal summer of El Niño decay years. By contrast, FTIC displays the persistence of a fully developed El Niño-like pattern during the same time period. Finally, CTRL exhibits an intermediate evolution between the above two extreme scenarios, despite that IOB warming is present in CTRL as in FSEIC. As a consequence, weak ISMs are simulated during both El Niño developing and decaying years in FTIC (and also in CTRL), while weak ISMs and El Niños tend to be followed systematically by normal/strong ISMs and La Niñas in FSEIC. Further analysis confirms that these differences in the decay phase of El Niño are responsible of the errors in the simulated ISM-ENSO lead-lag relationships in CTRL.

Overall, our results suggest that progresses or changes in the simulation of the ISM-ENSO relationships in CGCMs can be traced back to modifications of ENSO length and seasonal phase-locking related to the impact of the IOB on ENSO and details of its spatial structure (namely the equatorial SST gradient in the IO) during boreal winter. Surprisingly, the IOD or the direct relationship between IO SSTs and ISM only play a secondary role in modulating the ISM-ENSO relationship in our CGCM despite that it simulates an exaggerated IOD variability, with or without ENSO, as many current CGCMs (Cai and Cowan 2013; Li et al. 2016; Annamalai et al. 2017).

Our results are also fully consistent with the suggestion that a fast ENSO transition in the tropical Pacific and the persistence of IOB from boreal winter to boreal summer provide favorable conditions for the occurrence of a strong ISM (Yang et al. 2007, 2010; Boschat et al. 2011, 2012; Park et al. 2010; Chowdary et al. 2016, 2017). The emerging La Niña episode will strengthen the ISM circulation and the IOB warming will tend to enhance the local

evaporation, moisten the atmosphere and reduce the moist stability; all factors tend to increase ISM precipitation in FSEIC (Park et al. 2010).

5.b Discussion

In order to understand the physical processes, which are responsible of these different evolutions, it is important to highlight first that mean-state errors are the same in the different decoupled experiments analyzed here (Fig. 1a-d). This means that westward extension of cold tongue bias and of the El Niño pattern in the tropical Pacific, which have been identified as playing a seminal role in errors of the simulated ENSO decay pace and responsible of large inter-model spread in CMIP3 or CMIP5 models (Kug and Ham 2012; Tao et al. 2016; Li et al. 2019) cannot explain directly (or alone) the differences among the runs.

The crucial role of the IOB warming in hastening the El Niño to La Niña transition (well illustrated by the differences between the FTIC and CTRL) is consistent with previous studies (Watanabe and Jin 2002; Kug and Kang 2006; Ohba and Ueda 2007; Xie et al. 2009, 2016; Terray et al. 2016). On the other hand, the fact that the rapid decay of El Niño events and the emergence of a La Niña developing event are likely to be the effect of the spatial details of the IOB warming during boreal winter, rather than its simple existence or intensity per se, is an important result of the present study as many recent works suggest that the IOB capacitor effect is key mainly during the boreal summer of El Niño decay year, but not before (Chen et al. 2016; Li et al. 2017b).

By comparing further CTRL and FSEIC, it is demonstrated that the simulation skill of the ENSO decay pace and ISM-ENSO relationship is partly controlled by the (erroneous) SEIO SST variability simulated in the CGCM. As illustrated by Fig. 2b, this SST variability bias is characterized by an amplified seasonal cycle of SST variability with a double peak, one during boreal winter (e.g. February) and the other during boreal fall (e.g. September). Furthermore, Fig. 15b demonstrates that this erroneous double peak of SST variability in the SEIO is a bias shared by most CMIP5 models, despite SINTEX-F2 and CMIP5 models differ in their seasonal cycle of SST mean bias over SEIO (Figs. 2a and 15a). Most CMIP5 models exhibit a cold bias throughout the seasonal cycle in the SEIO while the SINTEX-F2 model exhibits a warm SST bias during boreal winter and a cold SST bias during boreal fall.

The cold SST mean bias and enhanced SST variability in the SEIO during boreal fall is a well-known and long-standing problem of both the SINTEX-F2 and CMIP5 models (Fischer et al. 2005; Terray et al. 2012; Prodhomme et al. 2014; Cretat et al. 2017; Cai and Cowan 2013; Li et al. 2015, 2016; Jourdain et al. 2016; Annamalai et al. 2017). Surprisingly, this

exaggerated SEIO SST variability during boreal fall, linked to the IOD, cannot explain the differences in ENSO evolution as described above.

On the other hand, the exaggerated SST variability in the SEIO during boreal winter in both SINTEX-F2 and CMIP5 models is less explored in the literature despite our analysis demonstrates its significant role on ENSO length and ISM-ENSO relationship. A working hypothesis for the existence of this SST bias is, however, the cold tongue bias and the associated excessive westward extension of El Niño SST warming along the equatorial Pacific found in most current CGCMs (Masson et al. 2012; Wang et al. 2014; Li and Xie 2012, 2014). These tropical Pacific biases have already been suggested to be very detrimental for a realistic simulation of both the ENSO-NWPA relationship and the negative IO feedback in CMIP5 models as they produce erroneous warm SST anomalies in the equatorial western Pacific during the El Niño decaying year, obstructing the formation of the anomalous NWPA (Kug and Ham 2012; Tao et al. 2016; Li et al. 2019). In order to investigate if the SEIO SST mean and variability biases are remotely forced by tropical Pacific errors in the SINTEX-F2 model, the annual cycle of monthly means and standard deviations of SEIO SSTs simulated in the FTPC and FTPC-obs decoupled experiments (see Section 2c) are displayed in Fig. 2. As ENSO variability is removed in both FTPC and FTPC-obs, but the Pacific mean-state errors are corrected only in FTPC-obs (Figs. 1e and 2a), the results suggest that SEIO biases during boreal fall have primarily local origins, as they are still present in both FTPC and FTPC-obs. On the other hand, those found during boreal winter are partly due to the remote Pacific forcing, as the erroneous SEIO SST variability during boreal winter is significantly damped in both FTPC and FTPC-obs, and the corresponding SST mean-state error is eliminated in FTPC-obs.

Thus, our results complement the previous studies, which focused primarily on the ocean-atmosphere and atmospheric processes over the equatorial western Pacific to explain the relationships between the ENSO decay pace, the NWPA and the local easterlies wind anomalies during boreal winter (Wang et al. 2000; Wu et al. 2017ab; Li et al. 2017b) and their degraded representation in current CGCMs (Kug and Ham 2012; Tao et al. 2016; Li et al. 2019). In SINTEX-F2, the negative IO feedback on ENSO is severely damped not only because of the local response (over the western equatorial Pacific) to the westward shift of the El Niño-related anomalies over the tropical Pacific, but also because such erroneous ENSO pattern produces an unrealistic remote forcing in the SEIO. The removal of the erroneous SEIO SST variability in FSEIC is sufficient to restore a realistic strength and position of the NWPA and associated equatorial easterlies and a correct ISM-ENSO relationship (Fig. 8)

related to the reduction of ENSO length. As most CMIP5 models exhibit exactly the same SST variability biases in the SEIO (Fig. 15a), it is not unlikely that correcting or removing the SEIO errors in these CGCMs will lead to similar improvements in their simulation of ENSO and ISM-ENSO relationships.

Past analysis of observations illustrate that the synchronous ISM-ENSO relationships has weakened, but that the impact of El Niño decaying phase on ISM has strengthened during recent decades (Fig 3; Yang et al. 2007, 2010; Boschat et al. 2012). This is fully consistent with the hypothesis of an enhanced negative IO feedback associated with the sustained IO warming (especially in the western IO), partly induced by anthropogenic forcing (Roxy et al. 2014) and the more frequent occurrence of the ENSO-related IO warming in recent decades (e.g., Boschat et al. 2012; Xie et al. 2016). Our numerical experiments do suggest that the IO is effectively an important climate element to explain the evolution of the ISM-ENSO system in the 20th century, as we are able to restore a realistic simulation of the lead-lag relationships between ISM and ENSO in a CGCM by simply eliminating the erroneous SST variability in the SEIO (Fig. 10a). In other words, it is conceivable that the intensified warming and negative feedback of the IO are important factors in the long-term variability of ENSO and ISM. This may have significant implications for our future projections of ENSO and ISM variations in a changing climate.

Additional testing with other CGCMs should therefore be performed in the future to promote a better understanding of the nature, seasonal timing and long-term behavior of the IO feedback on ENSO and ISM. However, the present work demonstrates that tropical SST biases in current CGCMs must be drastically reduced in order to shed new light on the mechanisms underlying the ISM variability. It is unlikely that state-of-the-art CGCMs will provide robust projections of ENSO or the ISM-ENSO relationship before prior reductions of systematic errors in the different tropical basins, like the cold tongue bias and the westward shift of the ENSO pattern in the tropical Pacific, the spurious IOD-like pattern in the IO or the unrealistic representation of the Atlantic zonal mode. Such systematic errors already preclude the robust attribution of the observed evolution of the ISM-ENSO relationships during the 20th century (illustrated in Fig. 3) to the anthropogenic forcing with the current CMIP5 simulations, as illustrated by the persistent controversies in the literature on this topic (Chen et al. 2010; Li and Ting 2015; Srivastava et al. 2015; Cash et al. 2017; Yun and Timmermann 2018; Feba et al. 2019; Bodai et al. 2020).

As illustrated in this work and summarized in two recent reviews (Cai et al. 2019; Wang 2019), interactions between the Indian, Pacific and also Atlantic basins play a seminal role in

explaining large-scale phenomena, like ENSO or ISM. From a modeling perspective, our results further highlight that remote SST mean-state and variability errors in one basin, for example the IO, can also interfere with SST biases in other basins like the Pacific and play a key-role in the simulation of ENSO or ISM in current CGCMs (see also Terray et al. 2016). In other words, this inter-basin framework is also fundamental to diagnose and correct the severe biases still affecting current CGCMs.

Appendix

The SST nudging is performed inside the SST equation of the ocean model. We suppressed the SST variability in a specific domain by applying a strong nudging of the SST toward a SST climatology computed from a control experiment or observations (see Table 1 and Section 2c for details). More precisely, this is done through a modification of the non-solar heat flux provided by the atmosphere to the ocean by adding a correction term that is proportional with the SST difference with the target climatology at each time step:

$$Q_{ns} = Q_{ns} + dq/dt * (SST - SST_{clim})$$

Q_{ns} : the nonsolar heat flux received from atmosphere

dq/dt : $-2400 \text{ W m}^{-2} \text{ K}^{-1}$ (corresponds to the heat flux needed to warm a 50m thick ocean layer of 1 K during 1 day)

SST_{clim} : the target SST daily climatology, after a linear interpolation at each time step of the day

The very strong dq/dt constant used here implies that the SST variability is almost suppressed in the selected domain. A Gaussian smoothing is finally applied in a transition zone in both longitude and latitude at the limits of the SST restoring domains (see Table 1).

This approach is interesting because the ocean dynamics (e.g. also thermocline variations) will be consistent with the SST in the ocean model, which is not the case when the SST is changed in the coupling interface of the coupled model as it is commonly done in many past/recent studies.

856 **Acknowledgments:** We gratefully acknowledge the outstanding work undertaken by the
857 many international modeling groups who provided their numerous model experiments for the
858 Program for Climate Model Diagnosis and Intercomparison (PCMDI). For more details on
859 model data or documentation for CMIP5, readers are referred to the PCMDI Web site
860 (<http://www-pcmdi.llnl.gov>). Pascal Terray is funded by Institut de Recherche pour le
861 Développement (IRD, France). KP Sooraj is funded by The Centre for Climate Change
862 Research (CCCR) and the Indian Institute of Tropical Meteorology (IITM), which are fully
863 funded by the Ministry of Earth Sciences, Government of India. The SINTEX-F2 simulations
864 are performed using HPC resources in France from GENCI-IDRIS (Grant 0106895 over the
865 last 5 years). The CFS simulation is performed using the HPC resources from IITM in India.
866 We finally acknowledge the two anonymous reviewers for their constructive comments.

References

- AchutaRao K, Sperber KR (2002) Simulation of the El Niño Southern Oscillation: Results from the Coupled Model Intercomparison Project. *Clim Dyn* 19:191-209
- AchutaRao K, Sperber KR (2006) ENSO simulation in coupled ocean-atmosphere models: are the current models better? *Clim Dyn* 27:1-15 DOI 10.1007/s00382-006-0119-7
- Achuthavarier D, Kirtman BP, Krishnamurty V, Huang B (2012) Role of the Indian Ocean in the ENSO-Indian Summer Monsoon Teleconnection in the NCEP Climate Forecast System. *J Clim* 25:2490-2508
- Alexander MA, Bladé I, Newman M, Lanzante JR, Lau NC, Scott JD (2002) The atmospheric bridge: the influence of ENSO teleconnections on air-sea interaction over the global oceans. *J Clim* 15:2205-2231
- Annamalai H, Xie SP, McCreary JP, Murtugudde R (2005) Impact of Indian Ocean Sea surface temperature on developing El Niño. *J Clim* 18:302-319
- Annamalai H, Hamilton K, Sperber KR (2007) The South Asian summer monsoon and its relationship with ENSO in the IPCC AR4 simulations. *J Clim* 20:1071-1092 <https://doi.org/10.1175/JCLI4035.1>.
- Annamalai H, Taguchi B, McCreary JP, Nagura M, Miyama T (2017) Systematic errors in South Asian monsoon simulation: Importance of equatorial Indian Ocean processes. *J Clim* 30:8159-8178
- Ashok K, Guan Z, Yamagata Y (2001) Impact of the Indian Ocean dipole on the relationship between the Indian monsoon rainfall and ENSO. *Geophys Res Lett* 28:4499-4502
- Ashok K, Guan Z, Saji NH, Yamagata T (2004), Individual and combined influences of ENSO and the Indian Ocean dipole on the Indian summer monsoon. *J Clim* 17:3141-3155
- Ashok K, Behera SK, Rao SA, Weng H, Yamagata T (2007) El Niño Modoki and its possible teleconnection. *J Geophys Res* 112:C11007
- Ashok K, Saji NH (2007) On the impacts of ENSO and Indian Ocean dipole events on sub-regional Indian summer monsoon rainfall. *Natural Hazards* 42:273-285
- Behera SK, Luo JJ, Masson S, Delecluse P, Gualdi S, Navarra A, Yamagata T (2005) Paramount impact of the Indian Ocean dipole on the East African short rains: a CGCM study. *J Clim* 18:4514-4530
- Behera SK, Luo JJ, Masson S, Rao SA, Sakuma H, Yamagata T (2006) A CGCM study on the interaction between IOD and ENSO. *J Clim* 19:1608-1705 doi: 10.1175/JCLI3797.1
- Bellenger H, Guilyardi E, Leloup J, Lengaigne M, Vialard J (2014) ENSO representation in

- climate models: from CMIP3 to CMIP5. *Clim Dyn* 42:1999-2018
- Bodai T, Drotos G, Herein M, Lunkeit F, Lurarini V (2020) The Forced Response of the El Niño-Southern Oscillation-Indian Monsoon Teleconnection in Ensembles of Earth System Models. *J Clim* 33:6 2163-2182
- Bollasina M, Ming Y (2013) The general circulation model precipitation bias over the southwestern equatorial Indian Ocean and its implications for simulating the South Asian monsoon. *Clim Dyn* 40:823-838
- Boschat G, Terray P, Masson S (2011) Interannual relationships between Indian summer monsoon and Indo-Pacific coupled modes of variability during recent decades. *Clim Dyn* 37:1019-1043 doi: 10.1007/s00382-010-0887-y
- Boschat G, Terray P, Masson S (2012) Robustness of SST teleconnections and precursory patterns associated with the Indian summer monsoon. *Clim Dyn* 38:2143-2165 doi: 10.1007/s00382-011-1100-7
- Cai W, Cowan T (2013) Why is the amplitude of the Indian Ocean dipole overly large in CMIP3 and CMIP5 climate models? *Geophys Res Lett* 40 :1200-1205 doi: 10.1002/grl.50208
- Cai W, Wu L, Lengaigne M, Li T, McGregor S, Kug J-S, Yu J-Y, Stuecker MF, Santoso A, Li X, Ham Y-G, Chikamoto Y, Ng B, McPhaden MJ, Du Y, Dommenges D, Jia F, Kajtar JB, Keenlyside, N., Lin, X., Luo, JJ, Martin-Rey M, Ruprich-Robert Y, Wang G, Xie SP, Yang Y, Kang SM, Choi J-Y, Gan B, Kim G-I, Kim C-E, Kim S, Kim J-H, Chang P (2019) Pan-tropical climate interactions. *Science* 363:6430 doi: 10.1126/science.aav4236
- Cash BA, Barimalala R, Kinter JL, Altshuler EL, Fennessy MJ, Manganello JV et al (2017) Sampling variability and the changing ENSO-monsoon relationship. *Clim Dyn* 48:4071-4079. <https://doi.org/10.1007/s00382-016-3320-3>
- Chen T-C (2003) Maintenance of summer monsoon circulations: a planetary-scale perspective. *J Climate* 16:2022-2037
- Chen W, Dong B, Lu R (2010), Impact of the Atlantic Ocean on the multidecadal fluctuation of El Niño-Southern Oscillation-South Asian monsoon relationship in a coupled general circulation model. *J Geophys Res* 115:D17109 doi:10.1029/2009JD013596
- Chen M-C, Li T, Shen X-Y et al. (2016) Relative roles of dynamic and thermodynamic processes in causing evolution asymmetry between El Niño and La Niña. *J Clim* 29:2201-2220 doi:10.1175/JCLI-D-15-0547.1
- Cherchi A, Gualdi S, Behera S, Luo JJ, Masson S, Yamagata, T, Navarra A (2007) The influence of tropical Indian Ocean SST on the Indian summer monsoon. *J Clim* 20:3083-3105 doi:10.1175/JCLI4161.1

959

960 Cherchi A, Navarra A (2013) Influence of ENSO and of the Indian Ocean Dipole on the
 961 Indian summer monsoon variability. *Clim Dyn* 41:81-103 doi:10.1007/s00382-012-1602-y
 962

963 Chowdary JS, Parekh A, Kakatkar R, Gnanaseelan C, Sriniva G, Singh P, Roxy M (2016)
 964 Tropical Indian Ocean response to the decay phase of El Nino in a coupled model and
 965 associated changes in south and east-Asian summer monsoon circulation and rainfall. *Clim*
 966 *Dyn* 47:831-844 doi:10.1007/s00382-015-2874-9
 967

968 Chowdary JS, Harsha HS, Gnanaseelan C, Srinivas G, Parekh A, Pillai, P, Naidu CV (2017)
 969 Indian summer monsoon rainfall variability in response to differences in the decay phase of El
 970 Niño. *Clim Dyn* 48:2707-2727
 971

972 Clarke AJ (2008) An Introduction to the Dynamics of El Niño and the Southern Oscillation.
 973 London: Academic Press pp 308
 974

975 Cleveland WS, Devlin SJ (1988) Locally Weighted Regression: An Approach to Regression
 976 Analysis by Local Fitting. *Journal of the American Statistical Association* 83:596-610
 977

978 Collins M and Coauthors (2010) The impact of global warming on the tropical Pacific Ocean
 979 and El Niño. *Nat Geosci* 3:391-397 doi:[10.1038/ngeo868](https://doi.org/10.1038/ngeo868)
 980

981 Cretat J, Terray P, Masson S, Sooraj KP, Roxy MK (2017) Indian Ocean and Indian Summer
 982 Monsoon: relationships without ENSO in ocean-atmosphere coupled simulations. *Clim Dyn*
 983 49:1429-1448 doi:10.1007/s00382-016-3387-x
 984

985 Cretat J, Terray P, Masson S, Sooraj KP (2018) Intrinsic precursors and timescale of the
 986 tropical Indian Ocean Dipole: Insights from partially decoupled experiment. *Clim Dyn*
 987 51:1311-1352 doi:10.1007/s00382-017-3956-7
 988

989 Doi T, Behera SK, Yamagata T (2016) Improved seasonal prediction using the SINTEX-F2
 990 coupled model. *JAMES* 8:1847-1867 doi:10.1002/2016MS000744
 991

992 Dommenges D, V Semenov and M Latif (2006) Impacts of the tropical Indian and Atlantic
 993 Oceans on ENSO. *Geophys Res Lett* 33:L11701 doi:10.1029/2006GL025871
 994

995 Drbohlav HKL, Gualdi S, Navarra A (2007) A diagnostic study of the Indian Ocean dipole
 996 mode in El Niño and non-El Niño years. *J Clim* 20:2961-2977 doi:10.1175/JCLI4153.1
 997

998 Ebisuzaki W (1997) A method to estimate the statistical significance of a correlation when the
 999 data are serially correlated. *J Clim* 10:2147-2153
 1000

1001 Feba F, Ashok K, Ravichandran M (2019) Role of changed Indo-Pacific atmospheric
 1002 circulation in the recent disconnect between the Indian summer monsoon and ENSO. *Clim*
 1003 *Dyn* 52:1461-1470
 1004

1005 Fischer A, Terray P, Guilyardi E, Delecluse P (2005) Two independent triggers for the Indian
1006 Ocean dipole/zonal mode in a coupled GCM. *J Clim* 18:3428-3449
1007

1008 Gadgil S, Vinayachandran PN, Francis PA, Gadgil S (2004) Extremes of the Indian summer
1009 monsoon rainfall, ENSO and equatorial Indian Ocean oscillation. *Geophys Res Lett*
1010 31:L12213 doi:10.1029/2004GL019733
1011

1012 Gadgil S, Rajeevan M, Nanjundiah R (2005) Monsoon prediction - why yet another failure?
1013 *Curr Sci* 84:1713-1719
1014

1015 Gadgil S, Rajeevan M, Francis PA (2007) Monsoon variability: links to major oscillations
1016 over the equatorial Pacific and Indian oceans. *Curr Sci* 93:182-194
1017

1018 Gershunov A, Schneider N, Barnett TP (2001) Low-frequency modulation of the ENSO-
1019 Indian monsoon rainfall relationship: Signal or noise? *J Clim* 14:2486-2492 [https://doi.org/](https://doi.org/10.1175/1520-0442(2001)014<2486:LFMOTE.2.0.CO;2)
1020 [10.1175/1520-0442\(2001\)014,2486:LFMOTE.2.0.CO;2](https://doi.org/10.1175/1520-0442(2001)014<2486:LFMOTE.2.0.CO;2).
1021

1022 Gill AE (1980) Some simple solutions for heat-induced tropical circulation. *Q J R Meteorol*
1023 *Soc* 106:447-462
1024

1025 Gu DJ, Li T, Ji ZP et al (2010) On the phase relations between the western North pacific,
1026 Indian, and Australian monsoons. *J Clim* 23:5572-5589 doi:10.1175/2010JCLI2761.1
1027

1028 Gualdi S, Guilyardi E, Navarra A, Masina S, Delecluse P (2003) The interannual variability
1029 in the tropical Indian Ocean as simulated by a CGCM. *Clim Dyn* 20:567-582
1030 doi:10.1007/s00382-002-0295-z
1031

1032 Ham YG, JS Kug (2014) ENSO phase-locking to the boreal winter in CMIP3 and CMIP5
1033 models. *Clim Dyn* 43:305-318
1034

1035 Huang B, Thorne Peter W et al (2017) Extended reconstructed sea surface temperature
1036 version 5 (ERSSTv5), upgrades, validations, and intercomparisons. *J Clim* 30:8179-8205
1037 <https://doi.org/10.1175/JCLI-D-16-0836.1>
1038

1039 Huffman GJ, Adler RF, Morrissey MM, Bolvin DT, Curtis S, Joyce R, McGavock B,
1040 Susskind J (2001) Global precipitation at one-degree daily resolution from multisatellite
1041 observations. *J Hydrometeor* 2:36-50
1042

1043 Izumo T, Vialard J, Lengaigne M et al (2010) Influence of the state of the Indian Ocean
1044 Dipole on the following years El Niño. *Nat Geosci* 3:168-172
1045

1046 Jansen MF, D Dommenget and N Keenlyside (2009) Tropical Atmosphere-Ocean Interactions
1047 in a Conceptual Framework. *J Clim* 22(3):550-567.
1048

1049 Jourdain NC et al (2013) The Indo-Australian monsoon and its relationship to ENSO and IOD

in reanalysis data and the CMIP3/CMIP5 simulations. *Clim Dyn* 41:3073-3102

Jourdain NC, Lengaigne M, Vialard J, Izumo T, Gupta AS (2016) Further insights on the influence of the Indian Ocean dipole on the following year's ENSO from observations and CMIP5 models. *J Clim* 29:637-658

Kajtar JB, Santoso A, England MH, Cai W (2017) Tropical climate variability: interactions across the Pacific, Indian, and Atlantic Oceans. *Clim Dyn* 48:2173-2190 doi:10.1007/s00382-016-3199-z

Keshavamurthy RN (1982) Response of the atmosphere to sea surface temperature anomalies over the equatorial Pacific and teleconnections of the Southern Oscillation. *J Atmos Sci*, 39, 1241-1259

Kinter JL III, Miyakoda K, Yang S (2002) Recent changes in the connection from the Asian monsoon to ENSO. *J Clim* 15:1203-1215 doi:10.1175/1520-0442(2002)015<1203:RCITCF>2.0.CO;2

Kirtman B and Shukla J (2000) Influence of the Indian summer monsoon on ENSO. *Q J R Meteor Soc* 126:213-239 doi:10.1002/qj.49712656211

Klein SA, Soden BJ, Lau NC (1999) Remote sea surface temperature variations during ENSO: evidence for a tropical atmospheric bridge. *J Clim* 12:917-932, doi:10.1175/1520-0442(1999)012<0917:RSSTVD>2.0.CO;2.

Kosaka Y, Xie S-P, Lau NC, Vecchi GA (2013) Origin of seasonal predictability for summer climate over the Northwestern Pacific. *PNAS* 110:7574-7579

Krishna Kumar K, Rajagopalan B, Cane MA (1999) On the weakening relationship between the Indian monsoon and ENSO. *Science* 284:2156-2159

Krishna Kumar K, Rajagopalan B, Hoerling M, Bates G, Cane M (2006) Unraveling the mystery of Indian monsoon failure during El Nino. *Science* 314:115-119.

Krishna RPM, Rao SA, Srivastava A et al (2019) Impact of convective parameterization on the seasonal prediction skill of Indian summer monsoon. *Clim Dyn* 53:6227-6243 <https://doi.org/10.1007/s00382-019-04921-y>

Krishnan R, Mujumdar M, Vaidya V, Ramesh KV, Satyan V (2003) The Abnormal Indian Summer Monsoon of 2000. *J Clim* 16:1177-1194

Krishnaswamy J, Vaidyanathan S, Rajagopalan B et al (2015) Non-stationary and non-linear influence of ENSO and Indian Ocean Dipole on the variability of Indian monsoon rainfall and extreme rain events. *Clim Dyn* 45:175-184 doi:10.1007/s00382-014-2288-0

1094

1095 Kucharski F, Bracco A, Yoo J, Molteni F (2007) Low- frequency variability of the Indian
 1096 monsoon-ENSO relationship and the tropical Atlantic: The weakening of the 1980s and
 1097 1990s. *J Clim* 20:4255-4266

1098

1099 Kucharski F, Bracco A, Yoo J, Molteni F (2008) Atlantic forced component of the Indian
 1100 monsoon interannual variability. *Geophysical Research Letters* 35:L04706

1101

1102 Kug J-S, Kang I-S (2006) Interactive feedback between ENSO and the Indian Ocean, *J Clim*
 1103 19:1784-1801

1104

1105 Kug J-S, Ham YG (2012) Indian Ocean feedback to the ENSO transition in a multi-model
 1106 ensemble. *J Clim* 25:6942-6957 doi: 10.1175/JCLI-D-12-00078.1

1107

1108 Lau NC, Nath MJ (2000) Impact of ENSO on the variability of the Asian-Australian
 1109 monsoons as simulated in GCM experiments. *J Clim* 13(24):4287-4309.

1110

1111 Lau NC, Nath MJ (2003) Atmosphere-ocean variations in the Indo-Pacific sector during
 1112 ENSO episode. *J Clim* 16:3-20 doi: 10.1175/1520-0442(2003)016<0003:AOVITI>2.0.CO;2

1113

1114 Lau NC, Wang B (2006) Interactions between the Asian monsoon and the El Niño/Southern
 1115 Oscillation. *The Asian Monsoon*, Wang B Ed, Springer/Praxis Publishing, New York, 478-
 1116 512.

1117

1118 Lau NC, Nath MJ (2012) A Model Study of the Air-Sea Interaction Associated with the
 1119 Climatological Aspects and Interannual Variability of the South Asian Summer Monsoon
 1120 Development. *J Clim* 25:839-857 doi: 10.1175/JCLI-D-11-00035.1

1121

1122 Levine RC, Turner AG, Marathayil D, Martin GM (2013) The role of northern Arabian Sea
 1123 surface temperature biases in CMIP5 model simulations and future projections of Indian
 1124 summer monsoon rainfall. *Clim Dyn* 4:155-172

1125

1126 Li G, Xie S-P (2012) Origins of tropical-wide SST biases in CMIP multi-model ensembles.
 1127 *Geophys Res Lett* 39:L22703. <https://doi.org/10.1029/2012G L0537 77>

1128

1129 Li G, Xie S-P (2014) Tropical biases in CMIP5 multimodel ensemble: the excessive
 1130 equatorial Pacific cold tongue and double ITCZ problems. *J Clim* 27:1765-1780

1131

1132 Li G, Xie S-P, Du Y (2015) Monsoon-induced biases of climate models in the tropical Indian
 1133 Ocean. *J Clim* 28:3058-3072 doi:10.1175/JCLI-D-14-00740.1

1134

1135 Li G, Xie S-P, Du Y (2016) A Robust but Spurious Pattern of Climate Change in Model
 1136 Projections over the Tropical Indian Ocean. *J Clim* 29 5589:5608

1137

1138 Li G, Xie S-P, He C et al (2017a) Western Pacific emergent constraint lowers projected
 1139 increase in Indian summer monsoon rainfall. *Nature Clim Change* 7:708-712

<https://doi.org/10.1038/nclimate3387>

Li G, Jian Y, Yang S et al (2019) Effect of excessive equatorial Pacific cold tongue bias on the El Niño-Northwest Pacific summer monsoon relationship in CMIP5 multi-model ensemble. *Clim Dyn* 52:6195-6212

Li T, Wang B, Chang C-P et al (2003) A theory for the Indian Ocean dipole-zonal mode. *J Atmos Sci* 60:2119-2135 doi:10.1175/1520-0469(2003)060<2119:ATFTIO>2.0.CO;2

Li T, Hsu P-C (2017) Monsoon dynamics and its interactions with ocean. *Fundamentals of Tropical Clim Dyn*, Springer International Publishing, Cham, 236 pp, doi:10.1007/978-3-319-59597-9.

Li T, Wang B, Wu B et al. (2017b) Theories on formation of an anomalous anticyclone in western North Pacific during El Niño: A review. *J. Meteor. Res.*, 31(6), 987-1006

Li X, Ting M (2015) Recent and future changes in the Asian monsoon-ENSO relationship: Natural or forced? *Geophys Res Lett* 42:3502-3512
<https://doi.org/10.1002/2015GL063557>

Li Z, Lin X, Cai W (2017c) Realism of modelled Indian summer monsoon correlation with the tropical Indo-Pacific affects projected monsoon changes. *Sci Rep* 7(1):1-7 doi: 10.1038/s41598-017-05225-z

Loschnigg J, Meehl GA, Webster PJ, Arblaster JM, Compo GP (2003) The Asian monsoon, the tropospheric biennial oscillation and the Indian Ocean dipole in the NCAR CSM. *J Clim* 16:2138-2158 doi:10.1175/1520-0442(2003)016<1617:TAMTTB>2.0.CO;2

Luo JJ, Masson S, Behera SK, Shingu S, Yamagata T (2005) Seasonal climate predictability in a coupled OAGCM using a different approach for ensemble forecasts. *J Clim* 18:4474-4497 doi:10.1175/JCLI3526.1

Luo JJ, Zhang R, Behera SK, Masumoto Y, Jin F-F, Lukas R, Yamagata T (2010) Interaction between El Niño and extreme Indian Ocean dipole, *J Clim* 23:726-742

Madec G (2008) NEMO ocean engine. Note du Pole de modelisation, Institut Pierre-Simon Laplace (IPSL) No 27. ISSN No 1288-1619

Masson S, Terray P, Madec G, Luo JJ, Yamagata T, Takahashi K (2012) Impact of intra-daily SST variability on ENSO characteristics in a coupled model. *Clim Dyn* 39:681-707

Meehl GA (1997) The south Asian monsoon and the tropospheric biennial oscillation (TBO). *J Clim* 10:1921-1943

Meehl GA, Arblaster JM (2002) The tropospheric biennial oscillation and the Asian-Australian monsoon rainfall. *J Clim* 15:722-744

1186

1187 Meehl GA, Arblaster JM, Loschnigg J (2003) Coupled ocean-atmosphere dynamical
 1188 processes in the tropical Indian and Pacific oceans and the TBO. *J Clim* 16:2138-2158
 1189 doi:10.1175/2767.1

1190

1191 Mooley DA, Parthasarathy B (1983) Variability of the Indian summer monsoon and tropical
 1192 circulation features. *Mon Wea Rev* 111:967-978

1193

1194 Morrison DF (1990) Multivariate statistical methods. McGraw-Hill, third edition, 495pp

1195

1196 Ohba M, Ueda H (2007) An Impact of SST Anomalies in the Indian Ocean in Acceleration of
 1197 the El Nino to La Nina Transition. *J Meteor Soc Jpn* 85:335-348
 1198

1199 Ohba M and M Watanbe (2012) Role of the Indo-Pacific Interbasin Coupling in Predicting
 1200 Asymmetric ENSO Transition and Duration. *J Clim*, 25, 3321-3334.
 1201

1202 Okumura YM, Ohba M, Deser C (2011) A proposed mechanism for asymmetric duration of
 1203 El Nino and La Nina. *J Clim* 24:3822-3829
 1204

1205 Pai DS, Sridhar L, Badwaik MR, Rajeevan M (2015) Analysis of the daily rainfall events
 1206 over India using a new long period (1901-2010) high resolution (0.25×0.25) gridded rainfall
 1207 data set. *Clim Dyn* 45:755-776

1208

1209 Park HS, Chiang JCH, Lintner BR and Zhang GJ (2010) The delayed effect of major El Niño
 1210 events on Indian monsoon rainfall. *J Clim* 23:932-946
 1211

1212 Parthasarathy B, Munot AA, Kothawale DR (1994) All-India monthly and seasonal rainfall
 1213 series: 1871-1993. *Theor Appl Climatol* 49:217-224
 1214

1215 Pillai PA, Annamalai H (2012) Moist dynamics of severe monsoons over South Asia: Role
 1216 of the tropical SST. *J Atmos Sci* 69(1):97-115
 1217

1218 Prodhomme C, Terray P, Masson S, Izumo T, Tozuka T, Yamagata T (2014) Impacts of
 1219 Indian Ocean SST biases on the Indian Monsoon: as simulated in a global coupled model.
 1220 *Clim Dyn* 42:271-290. doi:[10.1007/s00382-013-1671-6](https://doi.org/10.1007/s00382-013-1671-6)
 1221

1222 Prodhomme C, Terray P, Masson S, Boschat G, Izumo T (2015) Oceanic factors controlling
 1223 the Indian Summer Monsoon Onset in a coupled model. *Clim Dyn* 44:977-1002.
 1224 doi:[10.1007/s00382-014-2200-y](https://doi.org/10.1007/s00382-014-2200-y)
 1225

1226 Ramu DA, Chowdary JS, Ramakrishna SSVS, Kumar OSRUB (2018) Diversity in the
 1227 representation of large-scale circulation associated with ENSO-Indian summer monsoon
 1228 teleconnections in CMIP5 models. *Theor Appl Climatol* 132:465-478
 1229 <https://doi.org/10.1007/s00704-017-2092-y>
 1230

1231 Rao KG, Goswami BN (1988) Interannual variations of sea surface temperature over the
 1232 Arabian Sea and the Indian monsoon: a new perspective. *Mon Weath Rev* 116:558-568
 1233

1234 Rao, SA, and Coauthors (2019) Monsoon Mission: A targeted activity to improve Monsoon
 1235 prediction across scales. *BAMS*, Dec. 2019:2509-2532
 1236

1237 Rasmusson EM, Carpenter TH (1983) The relationship between eastern equatorial Pacific sea
 1238 surface temperature and rainfall over India and Sri Lanka. *Mon Wea Rev* 111:517-528
 1239 doi:10.1175/1520-0493(1983)111<0517:TRBEEP>2.0.CO;2
 1240

1241 Rayner NA, Parker DE, Horton EB, Folland CK, Alexander LV, Rowell DP, Kent EC,
 1242 Kaplan A (2003) Global analyses of sea surface temperature, sea ice, and night marine air
 1243 temperature since the late nineteenth century. *J Geophys Res* 108(D14)4407 doi:
 1244 10.1029/2002JD002670
 1245

1246 Reynolds RW, Smith TM, Liu C, Chelton DB, Casey KS, Schlax MG (2007) Daily high-
 1247 resolution-blended analyses for sea surface temperature. *J Clim* 20:5473-5496.
 1248 doi:10.1175/2007JCLI1824.1
 1249

1250 Rodwell MJ, Hoskins BJ (2001) Subtropical Anticyclones and Summer Monsoons. *J Clim*
 1251 14:3192-3211
 1252

1253 Roeckner E, Bäuml G, Bonaventura L, Brokopf R, Esch M, Giering M, Hagemann S,
 1254 Kirchner I, Kornblüth L, Manzini E, Rhodin A, Schlese U, Schulzweida U, Tompkins A
 1255 (2003) The atmospheric general circulation model ECHAM 5, Part I. MPI Report, vol 349.
 1256 Max-Planck-Institut für Meteorologie, Hamburg, pp 137
 1257

1258 Roxy MK, Rikita K, Terray P, Masson S (2014) The curious case of Indian Ocean Warming.
 1259 *J Clim* 27:8501-8508
 1260

1261 Sabeerali CT, Ajayamohan RS, Rao SA (2019) Loss of predictive skill of indian summer
 1262 monsoon rainfall in NCEP CFSv2 due to misrepresentation of Atlantic zonal mode. *Clim Dyn*
 1263 52:4599-4619 <https://doi.org/10.1007/s00382-018-4390-1>
 1264

1265 Saha SK, Pokhrel S, Salunke K, Dhakate A, Chaudhari HS, Rahaman H, Sujith K, Hazra A,
 1266 Sikka DR (2016) Potential predictability of Indian summer monsoon rainfall in NCEP CFSv2.
 1267 *JAMES* 8:96-120 <https://doi.org/10.1002/2015MS000542>
 1268

1269 Saha S et al (2014) The NCEP climate forecast system version 2. *J Clim* 27:2185-2208
 1270

1271 Saji NH, Goswami BN, Vinayachandran PN, Yamagata T (1999) A dipole mode in the
 1272 tropical Indian Ocean. *Nature* 401(6751):360-363. doi:[10.1038/43855](https://doi.org/10.1038/43855)
 1273

1274 Santoso A, England MH, Cai W (2012) Impact of Indo-Pacific Feedback Interactions on
 1275 ENSO Dynamics Diagnosed Using Ensemble Climate Simulations, *J Clim* 25:7743-7763
 1276

1277 Schott FA, Xie SP, McCreary JP (2009) Indian Ocean circulation and climate variability. *Rev*
 1278 *Geophys* 47:RG1002 doi:[10.1029/2007rg000245](https://doi.org/10.1029/2007rg000245)

1279
1280 Shukla J, Hagedorn R, Hoskins B, Kinter J, Marotzke J, Miller M, Palmer TN, Slingo J
1281 (2009) Strategies: Revolution in Climate Prediction is Both Necessary and Possible: A
1282 Declaration at the World Modelling Summit for Climate Prediction. *Bull Amer Meteor Soc*
1283 90:175-178.
1284
1285 Shukla RP, Huang B (2016) Interannual variability of the Indian summer monsoon associated
1286 with the air-sea feedback in the northern Indian Ocean. *Clim Dyn* 46:1977-1990
1287
1288 Sikka DR (1980) Some aspects of the large-scale fluctuations of summer monsoon rainfall
1289 over India in relations to fluctuations in the planetary and regional scale circulation
1290 parameters. *J Earth Syst Sci* 89:179-195 doi:10.1007/BF02913749
1291
1292 Spencer H, Sutton RT, Slingo JM, Roberts JM, Black E (2005) The Indian Ocean climate and
1293 dipole variability in the Hadley centre coupled GCMs. *J Clim* 18:2286-2307
1294
1295 Sperber KR, Annamalai, H, Kang I-S, Kitoh A, Moise A, Turner A, Wang B, Zhou T (2013)
1296 The Asian summer monsoon: an intercomparison of CMIP5 vs. CMIP3 simulations of the late
1297 20th century. *Clim Dyn* 41:2711-2744
1298
1299 Srivastava K, Srijith OP, Kshirsagar SR, Srivastava K (2015) Has modulation of Indian
1300 summer monsoon rainfall by sea surface temperature of the equatorial Pacific Ocean,
1301 weakened in recent years? *Clim Dyn* 45:2237-2254
1302
1303 Stuecker MF, Timmerman A, Jin FF, Chikamoto Y, Zhang W, Wittenberg AT, Widiastih E,
1304 Zhao S (2017) Revisiting ENSO/Indian Ocean dipole phase relationships. *Geophys Res Lett*
1305 44:2481-2492 doi: 10.1002/2016GL072308
1306
1307 Swapna and Coauthors (2015) The IITM earth system model. *Bull Amer MeteorSoc*
1308 96:1351–1367
1309
1310 Tao W, Huang G, Hu K et al (2016) A study of biases in simulation of the Indian Ocean basin
1311 mode and its capacitor effect in CMIP3/CMIP5 models. *Clim Dyn* 46:205-226
1312 <https://doi.org/10.1007/s00382-015-2579-0>
1313
1314 Taschetto AS, Gupta AS, Jourdain NC, Santoso A, Ummenhofer CC, England MH (2014)
1315 Cold tongue and warm pool ENSO events in CMIP5: mean state and future projections. *J*
1316 *Clim* 27:2861-2885
1317
1318 Taylor KE, Stouffer RJ, Meehl GA (2012) An overview of CMIP5 and the experiment design.
1319 *BAMS* 93:485-498.
1320
1321 Terao T, Kubota T (2005) East-west SST contrast over the tropical oceans and the post El
1322 Niño western North Pacific summer monsoon. *Geophys Res Lett* 32:L15706,
1323 doi:[10.1029/2005GL023010](https://doi.org/10.1029/2005GL023010).

1324

1325 Terray P (1995) Space/Time structure of monsoons interannual variability. *J Clim* 8:2595-
 1326 2619

1327

1328 Terray P, Delecluse P, Labattu S, Terray L (2003) Sea Surface Temperature Associations with
 1329 the Late Indian Summer Monsoon. *Clim Dyn* 21:593-618 DOI:10.1007/s00382-003-0354-0

1330

1331 Terray P, Guilyardi E, Fischer AS, Delecluse P (2005a) Dynamics of the Indian Monsoon and
 1332 ENSO Relationships in the SINTEX global Coupled Model. *Clim Dyn* 24:145-168
 1333 DOI:10.1007/s00382-004-0479-9

1334

1335 Terray P, Dominiak S, Delecluse P (2005b) Role of the southern Indian Ocean in the
 1336 transitions of the monsoon-ENSO system during recent decades. *Clim Dyn* 24:169-195 doi:
 1337 10.1007/s00382-004-0480-3

1338

1339 Terray P, Chauvin F, Douville H (2007) Impact of southeast Indian Ocean sea surface
 1340 temperature anomalies on monsoon-ENSO dipole variability in a coupled ocean-atmosphere
 1341 model. *Clim Dyn* 28:553-580 doi:10.1007/s00382-006-0192-y

1342

1343 Terray P, Kamala K, Masson S, Madec G, Sahai AK, Luo JJ, Yamagata T (2012) The role of
 1344 the intra-daily SST variability in the Indian monsoon variability and monsoon-ENSO-IOD
 1345 relationships in a global coupled model. *Clim Dyn* 39:729-754 doi:10.1007/s00382-011-
 1346 1240-9

1347

1348 Terray P, Masson S, Prodhomme C, Roxy MK, Sooraj KP (2016) Impacts of Indian and
 1349 Atlantic oceans on ENSO in a comprehensive modeling framework. *Clim Dyn* 46:2507-2533
 1350 doi: 10.1007/s00382-015-2715-x

1351

1352 Terray P, Sooraj KP, Masson S, Krishna RPM, Samson G, Prajeesh AG (2018) Towards a
 1353 realistic simulation of boreal summer tropical rainfall climatology in state-of-the art coupled
 1354 models: role of the background snow-free albedo. *Clim Dyn*, 50:3413-3439

1355

1356 Torrence C, Webster PJ (1999) Interdecadal changes in the ENSO-monsoon system. *J Clim*
 1357 12:2679-2690

1358

1359 Tourre y, White WB (1995) ENSO Signals in global upper-ocean temperature. *J Phys Ocean*
 1360 25:1317-1332

1361

1362 Turner AG, Annamalai H (2012) Climate change and the south Asian summer monsoon. *Nat*
 1363 *Clim Change* 2:1-9

1364

1365 Ummenhofer CC, Sen Gupta A, Li Y, Taschetto AS, England MH (2011) Multi-decadal

1366 modulation of the El Niño-Indian monsoon relationship by Indian Ocean variability. *Env Res*
1367 *Lett* 6:034,006
1368

1369 Valcke S (2006) OASIS3 user guide (prism_2-5). CERFACS technical report
1370 TR/CMGC/06/73, PRISM report no. 3, Toulouse, pp 64
1371

1372 Walker GT (1924) Correlation in seasonal variations of weather - A further study of world
1373 weather. *Mon Wea Rev* 53:252-254 doi:10.1175/1520-
1374 0493(1925)53<252:CISVOW>2.0.CO;2
1375

1376 Wang B (2006) *The Asian Monsoon*. Springer- Verlag/Praxis Publishing, New York, 787 pp.
1377

1378 Wang B, Wu RG, Fu XH (2000) Pacific-East Asian teleconnection: How does ENSO affect
1379 East Asian climate? *J Clim* 13:1517-1536 doi:10.1175/1520-
1380 0442(2000)013<1517:PEATHD>2.0.CO;2.
1381

1382 Wang B, Ding QH, Fu XH et al (2005) Fundamental challenge in simulation and prediction of
1383 summer monsoon rainfall. *Geophys Res Lett* 32:L15711 doi: 10.1029/2005GL02273412.
1384

1385 Wang B, Xiang BQ, Lee J-Y (2013) Subtropical high predictability establishes a promising
1386 way for monsoon and tropical storm predictions. *PNAS USA*, 110:2718-2722
1387 doi:10.1073/pnas.1214626110
1388

1389 Wang C (2019) Three- ocean interactions and climate variability: a review and perspective.
1390 *Clim Dyn* 53:5119-5136
1391

1392 Wang C, Zhang L, Lee SK et al (2014) A global perspective on CMIP5 climate model biases.
1393 *Nat Clim Chang* 4:201-205
1394

1395 Wang H, Murtugudde R, Kumar A (2016) Evolution of Indian Ocean dipole and its forcing
1396 mechanisms in the absence of ENSO. *Clim Dyn* 47:2481-2500 doi:10.1007/s00382-016-
1397 2977-y
1398

1399 Wang H, Kumar A, Murtugudde R, Narapusetty B, Seip K (2019) Covariations between the
1400 Indian Ocean dipole and ENSO: A modeling study. *Clim Dyn* 53:5743-5761 doi:
1401 10.1007/s00382-019-04895-x
1402

1403 Watanabe M, Jin F-F (2002) Role of Indian Ocean warming in the development of Philippine
1404 Sea anticyclone during ENSO. *Geophys Res Lett* 29:1478 doi: 10.1029/2001GL014318.
1405

1406 Webster PJ, Yang S (1992) Monsoon and ENSO: selectively interactive systems. *Q J R*
1407 *Meteor Soc* 118:877-926
1408

1409 Webster PJ, Hoyos CD (2010) Beyond the spring barrier? *Nat Geosci* 3:152-153 doi:
1410 10.1038/ngeo800

1411

1412 Webster PJ, Magana V, Palmer TN, Shukla J, Tomas RA, Yanai M, Yasunari T (1998)

1413 Monsoons: processes, predictability and the prospects for prediction. *J Geophys Res*

1414 103:14451-14510 doi:10.1029/97JC02719

1415

1416 Webster PJ, Moore AM, Loschnigg JP, Leben RR (1999) Coupled ocean-atmosphere

1417 dynamics in the Indian Ocean during 1997-1998. *Nature* 401:356-360 doi:10.1038/43848

1418

1419 Wieners CE, Dijkstra HA, de Ruijter WPM (2017a) The influence of the Indian Ocean on

1420 ENSO stability and flavor. *J Clim* 30:2601-2620 doi:10.1175/JCLI-D-16-0516.1

1421

1422 Wieners CE, Dijkstra HA, de Ruijter WPM (2017b) The influence of atmospheric convection

1423 on the interaction between the Indian Ocean and ENSO. *J Clim* 30:10155-10178

1424 doi:10.1175/JCLI-D-17-0081.1

1425

1426 Wu B, Zhou TJ, Li T (2017a) Atmospheric dynamic and thermodynamic processes driving

1427 the western North Pacific anomalous anticyclone during El Niño. Part I: Maintenance

1428 mechanisms. *J Clim* 30:9621-9635 doi:10.1175/JCLID-16-0489.1

1429

1430 Wu B, Zhou TJ, Li T (2017b) Atmospheric dynamic and thermodynamic processes driving

1431 the western North Pacific anomalous anticyclone during El Niño. Part II: Formation

1432 processes. *J Clim* 30:9637-9650 doi:10.1175/JCLI-D-16-0495.1

1433

1434 Wu R, Kirtman BP (2004a) Impacts of the Indian Ocean on the Indian summer monsoon-

1435 ENSO relationship. *J Clim* 17:3037-3054

1436

1437 Wu R, Kirtman BP (2004b) Understanding the impacts of the Indian Ocean on ENSO

1438 variability in a coupled GCM. *J Clim* 17:4019-4031

1439

1440 Wu R, Kirtman BP (2005) Roles of Indian and Pacific Ocean air-sea coupling in tropical

1441 atmospheric variability. *Clim Dyn* 25:155-170

1442

1443 Wu R, Chen J, Chen W (2012) Different types of ENSO influences on the Indian summer

1444 monsoon variability. *J Clim* 25:903-920 <https://doi.org/10.1175/JCLI-D-11-00039.1>.

1445

1446 Xie SP, Hu K, Hafner J et al (2009) Indian Ocean capacitor effect on Indo-Western pacific

1447 climate during the summer following El Niño. *J Clim* 22:730-747 doi:

1448 10.1175/2008JCLI2544.1.

1449

1450 Xie SP, Kosaka Y, Du Y et al (2016) Indo-western Pacific Ocean capacitor and coherent

1451 climate anomalies in post-ENSO summer: a review. *Adv Atmos Sci* 33:411-432 doi:

1452 10.1007/s00376-015-5192-6

1453

1454 Yang JL, Liu QY, Xie S-P, et al (2007) Impact of the Indian Ocean SST basin mode on the

1455 Asian summer monsoon. *Geophys Res Lett* 34:L02708 doi:10.1029/2006GL028571

1456

1457 Yang J, Liu Q, Liu Z (2010) Linking Observations of the Asian Monsoon to the Indian Ocean
1458 SST: Possible Roles of Indian Ocean Basin Mode and Dipole Mode. *J Clim* 23:5889-5902
1459
1460 Yang Y, Xie SP, Wu L, Kosaka Y, Lau NC, Vecchi GA (2015) Seasonality and predictability
1461 of the Indian Ocean Dipole mode: ENSO forcing and internal variability. *J Clim* 28:8021-
1462 8036
1463
1464 Yasunari T (1990) Impact of Indian monsoon on the coupled atmosphere/ocean system in the
1465 tropical Pacific. *Meteor & Atmos Phys* 44:29-41
1466
1467 Yun KS, Timmermann A (2018) Decadal monsoon-ENSO relationships reexamined.
1468 *Geophys Res Lett* 45:2014-2021 <https://doi.org/10.1002/2017GL076912>
1469
1470 Zhou Q, Duan W, Mu M, Feng R (2015) Influence of positive and negative Indian Ocean
1471 dipoles on ENSO via the Indonesian throughflow: results from sensitivity experiments. *Adv*
1472 *Atmos Sci* 32:783-793
1473
1474 Zhu J, Shukla J (2013) The Role of Air-Sea Coupling in Seasonal Prediction of Asia-Pacific
1475 Summer Monsoon Rainfall. *J Clim* 26:5689-5697 DOI:10.1175/JCLI-D-13-00190.1
1476

Figure captions

Figure 1: **a)** SST means difference ($^{\circ}\text{C}$) between CTRL (years 11-210) and HadISST1.1 dataset (years 1979-2012); **b)** SST means difference ($^{\circ}\text{C}$) between FTPC (years 11-110) and CTRL; **c)** SST means difference ($^{\circ}\text{C}$) between FTIC (years 11-110) and CTRL; **d)** SST means difference ($^{\circ}\text{C}$) between FSEIC (years 11-60) and CTRL and **e)** SST means difference ($^{\circ}\text{C}$) between FTPC-obs (years 11-50) and CTRL. The nudging domains for FTPC, FTIC and FSEIC experiments are shown, respectively, in panels b (blue), c (green) and d (purple).

Figure 2: **a)** Monthly means of the SEIO (90°E - 115°E and 0°S - 10°S ; unit: $^{\circ}\text{C}$) SST time series from HadISST1.1 dataset (for the 1950-2012 and 1979-2012 periods) and the CTRL, FSEIC, FTPC and FTPC-obs experiments performed with the SINTEX-F2 model; **b)** Monthly standard deviations of the SEIO SST time series (unit: $^{\circ}\text{C}$) from HadISST1.1 dataset (for the 1950-2012 and 1979-2012 periods) and the CTRL, FSEIC, FTPC and FTPC-obs experiments.

Figure 3: **a)** Lead-lag correlations between AIR time series and bi-monthly Niño-3.4 SSTs for different time periods, starting from the beginning of the previous year (e.g. year - 1) to the end of the following year of the monsoon (e.g. year +1) and **b)** Same as **a)** but using the ISMR time series derived from the IMD dataset. X-axis indicates the lag (in 2 months interval) for a 36 months period starting one year before the developing year of ISM and Y-axis is the amplitude of the correlation. Thus, the coefficients corresponding to -1, 0, +1 month lags refer, respectively, to the correlations between AIR in year 0 (e.g. JJAS ISM rainfall) and April-May, June-July and August-September Niño-3.4 SSTs, also during year 0, and so on. Lead-lag correlations between ISMR time series estimated from GPCP dataset and bi-monthly Niño-3.4 SSTs for the period 1979-2012 are also displayed in panels **a** and **b** for comparison. All time series are detrended with a LOESS method (Cleveland and Devlin 1988). Black diamond symbols indicate correlations that are above the 95% significance confidence level according to a phase-scrambling bootstrap test (Ebisuzaki 1997) with 999 samples.

Figure 4: **a)** Lead-lag correlations between ISMR time series and bi-monthly Niño-3.4 SSTs, starting from the beginning of the previous year (e.g. year - 1) to the end of the following year of the monsoon (e.g. year +1) as simulated in the control experiments (CTRL) of the

SINTEX-F2 and CFSv2 models and observed during the period 1979-2012. All time series are detrended with a LOESS method (Cleveland and Devlin 1988). Black diamond symbols indicate correlations that are above the 95% significance confidence level according to a phase-scrambling bootstrap test (Ebisuzaki 1997) with 999 samples. For observations, GPCP and HadISST1.1 datasets are used, respectively, for estimating the ISMR and Niño-3.4 SST time series; **b)** Monthly standard deviations of the Niño-3.4 SST time series from HadISST1.1 dataset (for the 1950-2012 and 1979-2012 periods) and the CTRL experiments of the SINTEX-F2 and CFSv2 models; **c)** Monthly standard deviations of the ISMR time series from GPCP dataset (for 1979-2012 period) and the CTRL experiments of the SINTEX-F2 and CFSv2 models; **d)** Monthly means of the ISMR time series from GPCP dataset (for 1979-2012 period) and the CTRL experiments of the SINTEX-F2 and CFSv2 models.

Figure 5: Same as Fig. 4, but for historical runs of 25 CMIP5 models. For CMIP models, the period 1950-2000 is considered and time series are only linearly detrended. Statistical significance is not plotted, but correlation coefficients with an absolute value greater than 0.25 are above the 95% significance confidence level according to a Student two-tailed t test. For observations, GPCP and HadISST1.1 datasets are used, respectively, for estimating the ISMR and Niño-3.4 SST time series. The ensembles mean and spread across the CMIP5 models are also displayed. The spread is computed as the ensemble mean plus and minus the ensemble standard deviation (thick black circles in all panels).

Figure 6: **(a, b)** June-July and August-September mean rainfall (shading) and 850-hPa wind (vectors) anomalies regressed against the ISMR index (e.g. JJAS ISM rainfall) in the CTRL experiment; **(c, d)** same as **(a, b)** but for the FTPC experiment; **(e, f)** same as **(a, b)** but for the FTIC experiment and **(g, h)** same as **(a, b)** but for the FSEIC experiment. Unit for the rainfall and 850-hPa wind regression coefficients are, respectively, in mm/day by mm/day and m/s by mm/day. Only rainfall and 850-hPa wind regression coefficients above the 95% significance confidence level according to a phase-scrambling bootstrap test (Ebisuzaki 1997) with 999 samples are shown.

Figure 7: **(a, b, c, d, e, f)** correlation coefficients between the ISMR index (e.g. JJAS ISM rainfall) and bi-monthly SST anomalies from February-March to December-January of year 0 in the FTPC experiment. **(g, h, i, j, k, l)** same as **(a, b, c, d, e, f)** but for bi-monthly 200-hPa

velocity potential anomalies. Correlation coefficients above the 95% significance confidence level according to a phase-scrambling bootstrap test (Ebisuzaki 1997) with 999 samples are contoured. In (a, b, c, d, e, f), correlation coefficients in the Pacific nudging domain are masked.

Figure 8: Same as Fig. 4, but for the FTIC and FSEIC experiments done with the SINTEX-F2 model. The results for the control (CTRL) and FTIC experiments performed with the SINTEX-F2 model are also displayed for comparison (only in panels c and d for FTIC).

Figure 9: Power spectra of Niño-3.4 SST anomalies for CTRL (red), FTIC (green) and FSEIC (blue) experiments. The bottom axis is the period (unit: year), the left axis is variance (unit: $^{\circ}\text{C}^2$) and both axes are in logarithm scale. Dashed red curves show the point-wise 95% confidence limits for the Niño-3.4 SST spectrum estimated from the CTRL experiment.

Figure 10: a) bi-monthly SST anomalies regressed against the December-January Niño-3.4 SST time series for the following February-March, April-May, June-July, August-September and October-November (e.g. in year +1) in the CTRL experiment; b) same as a) but for the FTIC experiment; c) same as a) but for the FSEIC experiment. Unit for the SST regression coefficients is in K by K. Regression coefficients reaching the 10% significance level according to a phase-scrambling bootstrap test (Ebisuzaki 1997) with 999 samples are contoured.

Figure 11: a) bi-monthly mean rainfall (shading) and 850-hPa wind (vectors) anomalies regressed against the December-January Niño-3.4 SST time series for the following February-March, April-May, June-July, August-September and October-November (e.g. in year +1) in the CTRL experiment; b) same as a) but for the FTIC experiment; c) same as a) but for the FSEIC experiment. Unit for the rainfall and 850-hPa wind regression coefficients are, respectively, in mm/day by K and m/s by K. Only rainfall and 850-hPa wind regression coefficients reaching the 10% significance level according to a phase-scrambling bootstrap test (Ebisuzaki 1997) with 999 samples are shown.

Figure 12: **a)** bi-monthly mean 20°C isotherm depth (a proxy for thermocline depth) anomalies regressed against the December-January Niño-3.4 SST time series for the following February-March, April-May, June-July, August-September and October-November (e.g. in year +1) in the CTRL experiment; **b)** same as **a)** but for the FTIC experiment; **c)** same as **a)** but for the FSEIC experiment. Unit for the 20°C isotherm depth regression coefficients is in m by K. Regression coefficients reaching the 10% significance level according to a phase-scrambling bootstrap test (Ebisuzaki 1997) with 999 samples are contoured.

Figure 13: **(a, b, c, d)** February-March 850-hPa stream function, 850-hPa velocity potential, 200-hPa velocity potential and 850-hPa zonal wind anomalies regressed against the preceding December-January Niño-3.4 SST time series in the CTRL experiment; **(e, f, g, h)** same as **(a, b, c, d)** but for the FTIC experiment; **(i, j, k, l)** same as **(a, b, c, d)** but for the FSEIC experiment. Units for the stream function and velocity potential regression coefficients are in $10^5 \text{ m}^2 \text{ s}^{-1}$ by K and for 850-hPa zonal wind in m s^{-1} by K. Regression coefficients reaching the 10% significance level according to a phase-scrambling bootstrap test (Ebisuzaki 1997) with 999 samples are contoured.

Figure 14: **(a, b)** June-July and August-September 200-hPa velocity potential anomalies regressed against the preceding December-January Niño-3.4 SST time series in the CTRL experiment; **(c, d)** same as **(a, b)** but for the FTIC experiment; **(e, f)** same as **(a, b)** but for the FSEIC experiment. Units for the velocity potential regression coefficients are in $10^5 \text{ m}^2 \text{ s}^{-1}$ by K. Regression coefficients reaching the 10% significance level according to a phase-scrambling bootstrap test (Ebisuzaki 1997) with 999 samples are contoured.

Figure 15: **a)** Monthly means of the SEIO (90°E-115°E and 0°S-10°S; unit: °C) SST time series from HadISST1.1 dataset and the historical runs of 25 CMIP5 models; **b)** Monthly standard deviations of the SEIO SST time series from HadISST1.1 dataset and the historical runs of 25 CMIP5 models. All observed and simulated statistics are estimated from the period 1950-2000. The ensemble mean and spread across the CMIP5 models are also displayed. The spread is computed as the ensemble mean plus and minus the ensemble standard deviation (thick black circles in panels **a** and **b**).

1606 **Figure S1:** (a, b, c, d, e, f) correlation coefficients between the ISMR index (e.g. JJAS ISM
1607 rainfall) and bi-monthly SST anomalies from February-March to December-January of year 0
1608 in the CTRL experiment. (g, h, i, j, k, l) same as (a, b, c, d, e, f) but for bi-monthly 200 hPa
1609 velocity potential anomalies. Correlation coefficients above the 95% significance confidence
1610 level according to a phase-scrambling bootstrap test (Ebisuzaki 1997) with 999 samples are
1611 contoured.
1612

Table captions

Table 1: Summary of the numerical experiments with their main characteristics, including length, nudging domain and SST climatology used for the nudging in the Indian or Pacific oceans decoupled experiments. The nudged experiments are the Forced Tropical Pacific Climatology (FTPC) run, the Forced Tropical Indian Climatology (FTIC) run, the Forced South-East Indian Climatology (FSEIC) run and, finally, the Forced Tropical Pacific observed Climatology (FTPC-obs) run. See text for more details. For the FTPC and FTPC-obs experiments only ocean grid-points in the Pacific are included in the correction or smoothing areas and, similarly, for the FTIC and FSEIC experiments for their respective domains. The different correction domains are also displayed in Figure 1b-d. The observed SST climatology used in the FTPC-obs experiment is derived from the AVHRR only daily Optimum Interpolation SST version 2 (OISSTv2) dataset for the 1982-2010 period (Reynolds et al. 2007).

Table S1: Description of the 25 Coupled Model Inter-comparison Project phase 5 (CMIP5) models used in our analysis. We use the historical coupled model experiments contributing to CMIP5 (see, url: <http://pcmdi9.llnl.gov>). Here, the first member of each model's ensemble of historical runs is used for all the analysis performed using CMIP5 models (e.g. Figures 5) and computations are done for the period 1950-2000. Each model dataset has been re-gridded into a $2.5^{\circ} \times 2.5^{\circ}$ horizontal grid, using a first-order remapping procedure implemented in the Climate Data Operators (<https://code.zmaw.de/projects/cdo>), before processing.

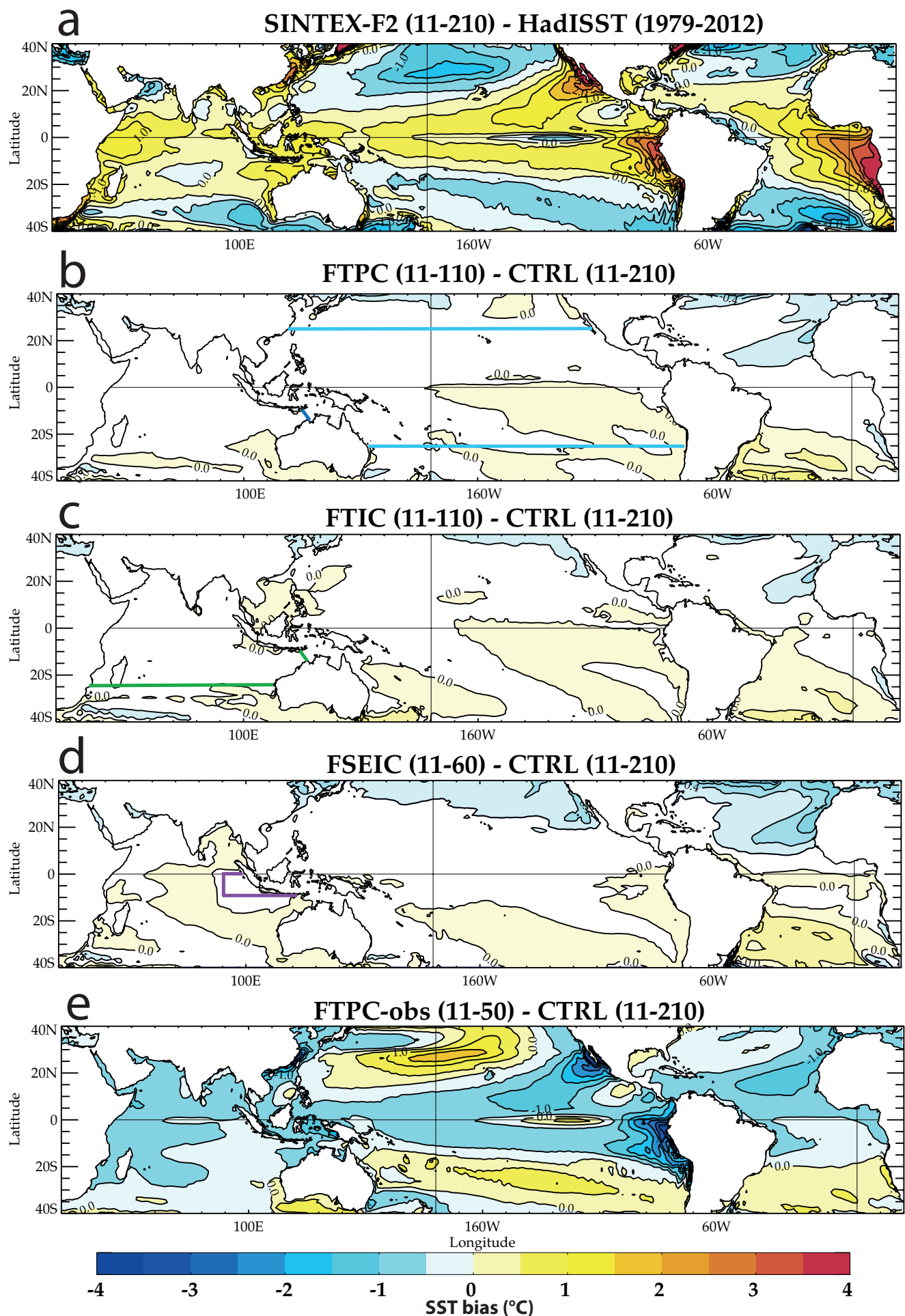


Figure 1: **a)** SST means difference ($^{\circ}\text{C}$) between CTRL (years 11-210) and HadISST1.1 dataset (years 1979-2012); **b)** SST means difference ($^{\circ}\text{C}$) between FTPC (years 11-110) and CTRL; **c)** SST means difference ($^{\circ}\text{C}$) between FTIC (years 11-110) and CTRL; **d)** SST means difference ($^{\circ}\text{C}$) between FSEIC (years 11-60) and CTRL and **e)** SST means difference ($^{\circ}\text{C}$) between FTPC-obs (years 11-50) and CTRL. The nudging domains for FTPC, FTIC and FSEIC experiments are shown, respectively, in panels b (blue), c (green) and d (purple).

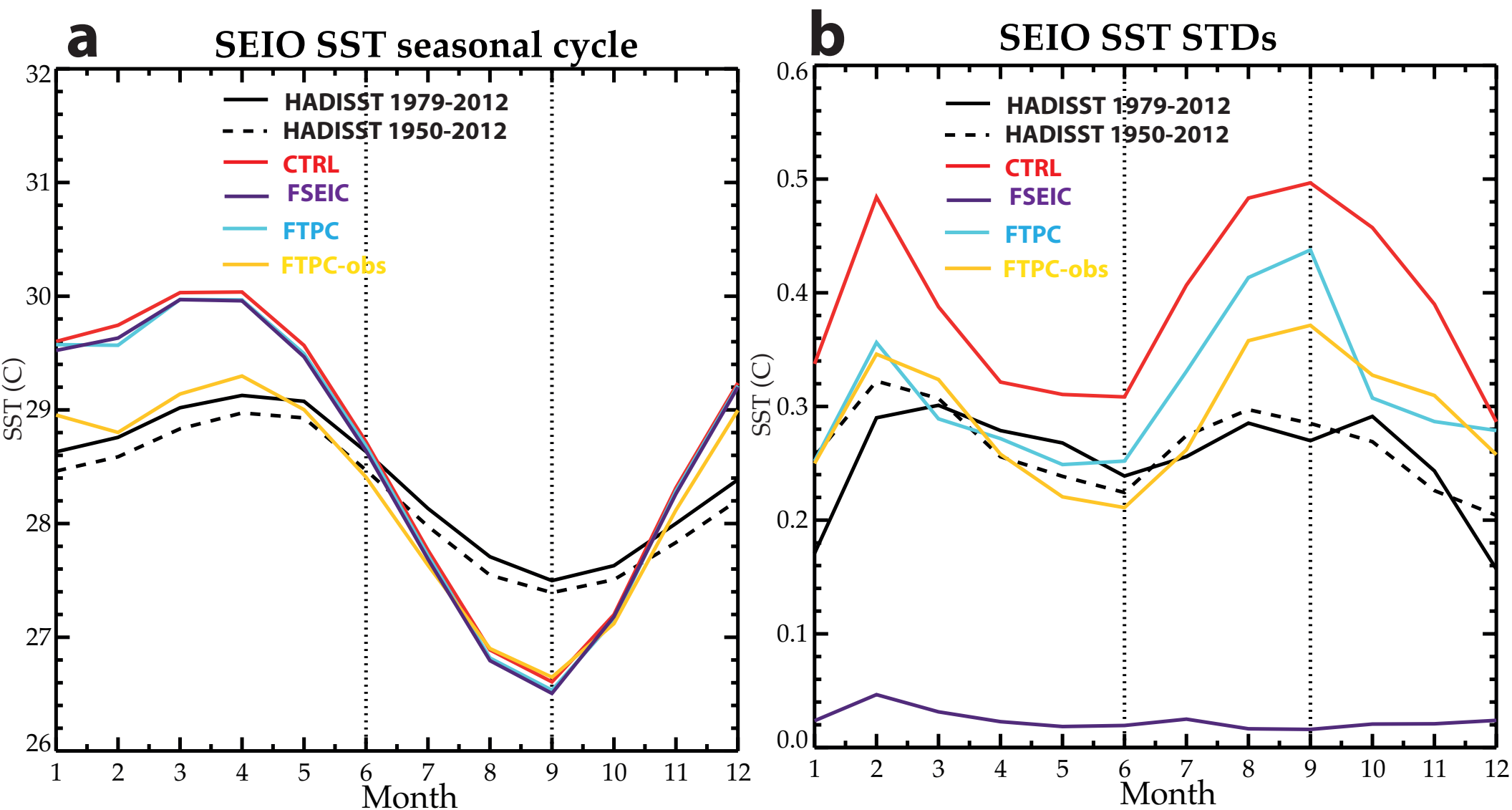


Figure 2: **a)** Monthly means of the SEIO (90°E - 115°E and 0°S - 10°S ; unit: $^{\circ}\text{C}$) SST time series from HadISST1.1 dataset (for the 1950-2012 and 1979-2012 periods) and the CTRL, FSEIC, FTPC and FTPC-obs experiments performed with the SINTEX-F2 model; **b)** Monthly standard deviations of the SEIO SST time series (unit: $^{\circ}\text{C}$) from HadISST1.1 dataset (for the 1950-2012 and 1979-2012 periods) and the CTRL, FSEIC, FTPC and FTPC-obs experiments.

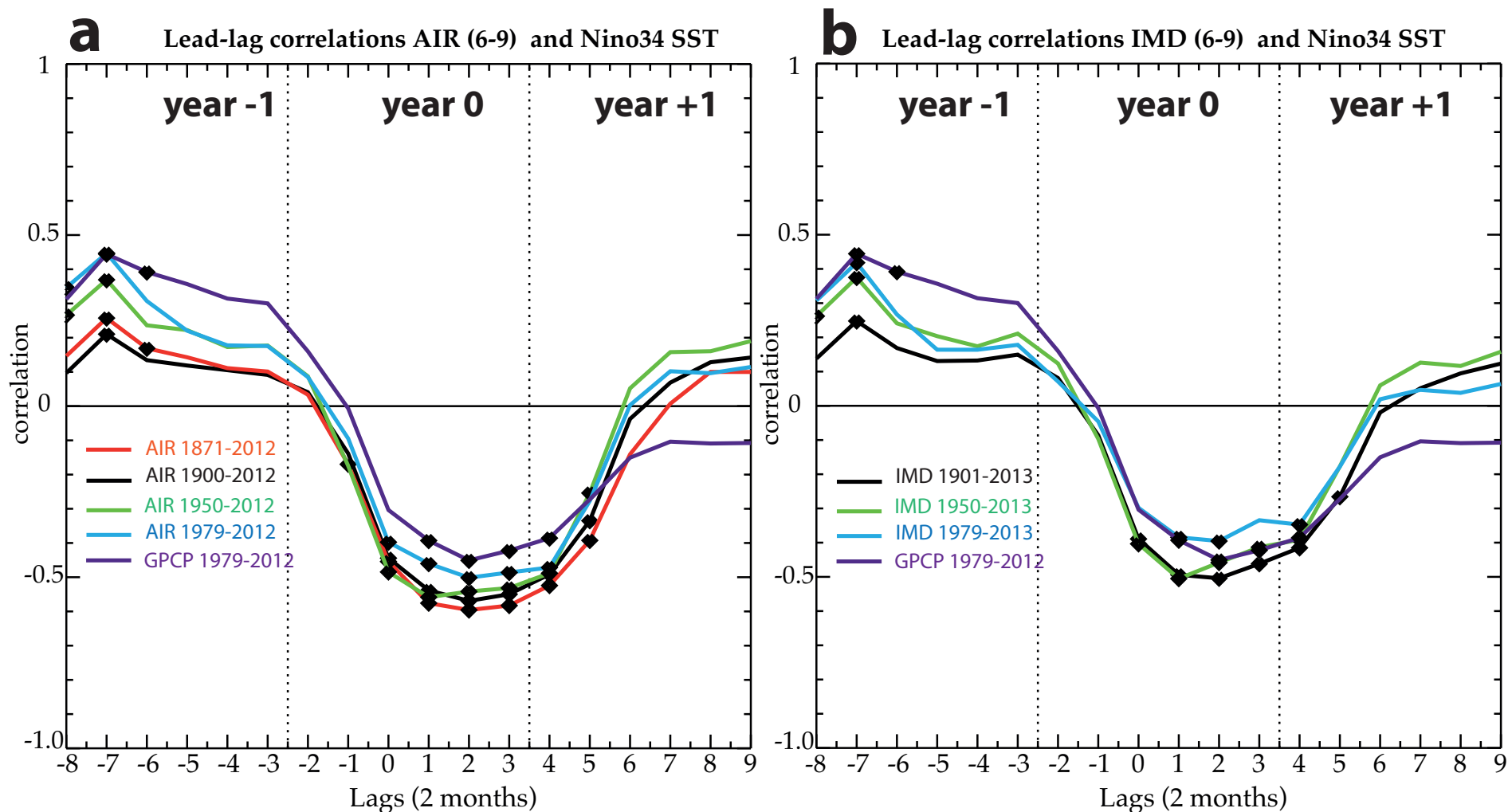


Figure 3: a) Lead-lag correlations between AIR time series and bi-monthly Niño-3.4 SSTs for different time periods, starting from the beginning of the previous year (e.g. year - 1) to the end of the following year of the monsoon (e.g. year +1) and **b)** Same as **a)** but using the ISMR time series derived from the IMD dataset. X-axis indicates the lag (in 2 months interval) for a 36 months period starting one year before the developing year of ISM and Y-axis is the amplitude of the correlation. Thus, the coefficients corresponding to -1, 0, +1 month lags refer, respectively, to the correlations between AIR in year 0 (e.g. JJAS ISM rainfall) and April-May, June-July and August-September Niño-3.4 SSTs, also during year 0, and so on. Lead-lag correlations between ISMR time series estimated from GPCP dataset and bi-monthly Niño-3.4 SSTs for the period 1979-2012 are also displayed in panels a and b for comparison. All time series are detrended with a LOESS method (Cleveland and Devlin 1988). Black diamond symbols indicate correlations that are above the 95% significance confidence level according to a phase-scrambling bootstrap test (Ebisuzaki 1997) with 999 samples.

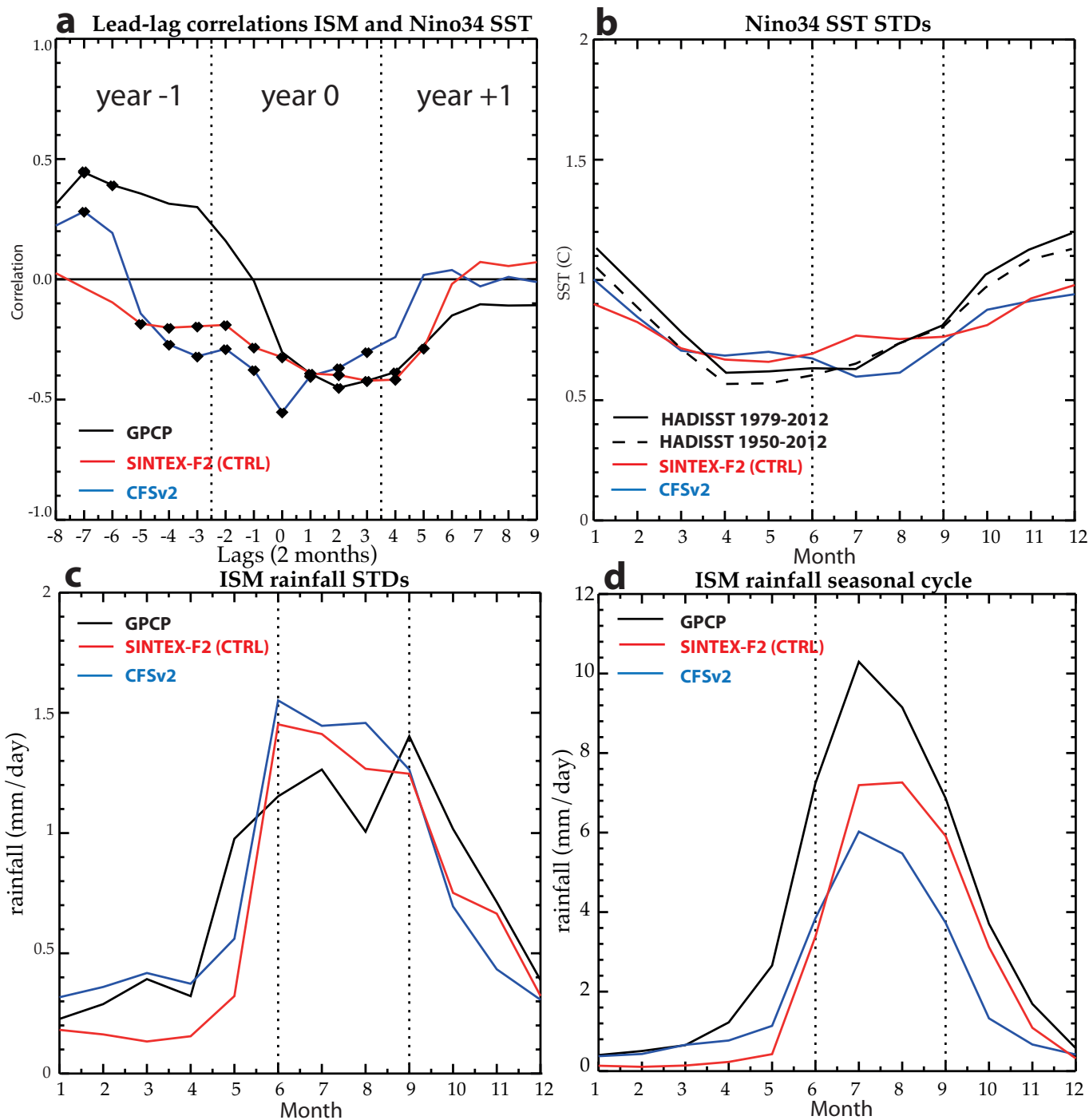


Figure 4: **a)** Lead-lag correlations between ISMR time series and bi-monthly Niño-3.4 SSTs, starting from the beginning of the previous year (e.g. year - 1) to the end of the following year of the monsoon (e.g. year +1) as simulated in the control experiments (CTRL) of the SINTEX-F2 and CFSv2 models and observed during the period 1979-2012. All time series are detrended with a LOESS method. Black diamond symbols indicate correlations that are above the 95% significance confidence level according to a phase-scrambling bootstrap test (Ebisuzaki 1997) with 999 samples. For observations, GPCP and HadISST1.1 datasets are used, respectively, for estimating the ISMR and Niño-3.4 SST time series; **b)** Monthly standard deviations of the Niño-3.4 SST time series from HadISST1.1 dataset (for the 1950-2012 and 1979-2012 periods) and the CTRL experiments of the SINTEX-F2 and CFSv2 models; **c)** Monthly standard deviations of the ISMR time series from GPCP dataset (for 1979-2012 period) and the CTRL experiments of the SINTEX-F2 and CFSv2 models; **d)** Monthly means of the ISMR time series from GPCP dataset (for 1979-2012 period) and the CTRL experiments of the SINTEX-F2 and CFSv2 models.

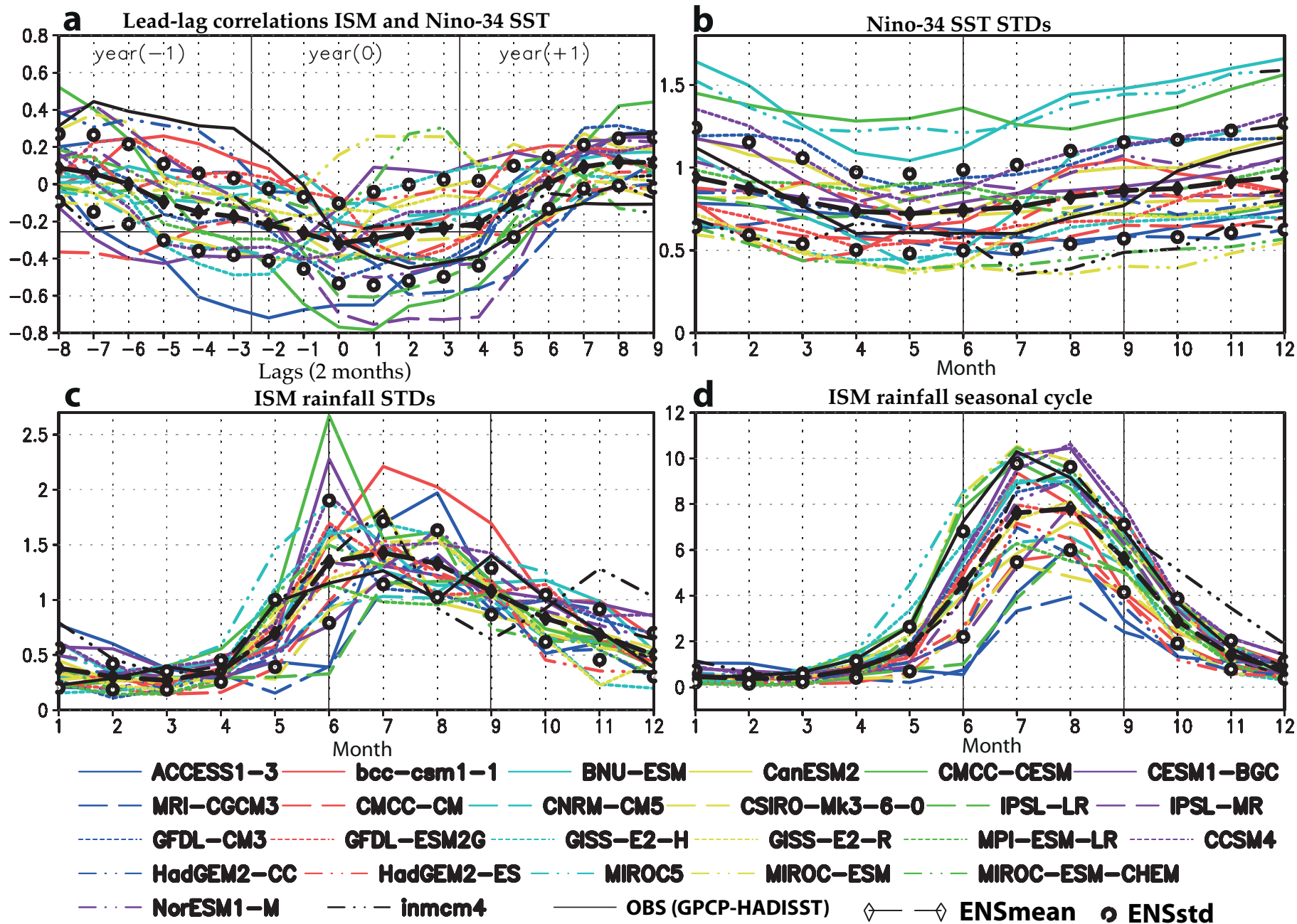


Figure 5: Same as Fig. 4, but for historical runs of 25 CMIP5 models. For CMIP models, the period 1950-2000 is considered and time series are only linearly detrended. Statistical significance is not plotted, but correlation coefficients with an absolute value greater than 0.25 are above the 95% significance confidence level according to a Student two-tailed t test. For observations, GPCP and HadISST1.1 datasets are used, respectively, for estimating the ISMR and Niño-3.4 SST time series. The ensembles mean and spread across the CMIP5 models are also displayed. The spread is computed as the ensemble mean plus and minus the ensemble standard deviation (thick black circles in all panels).

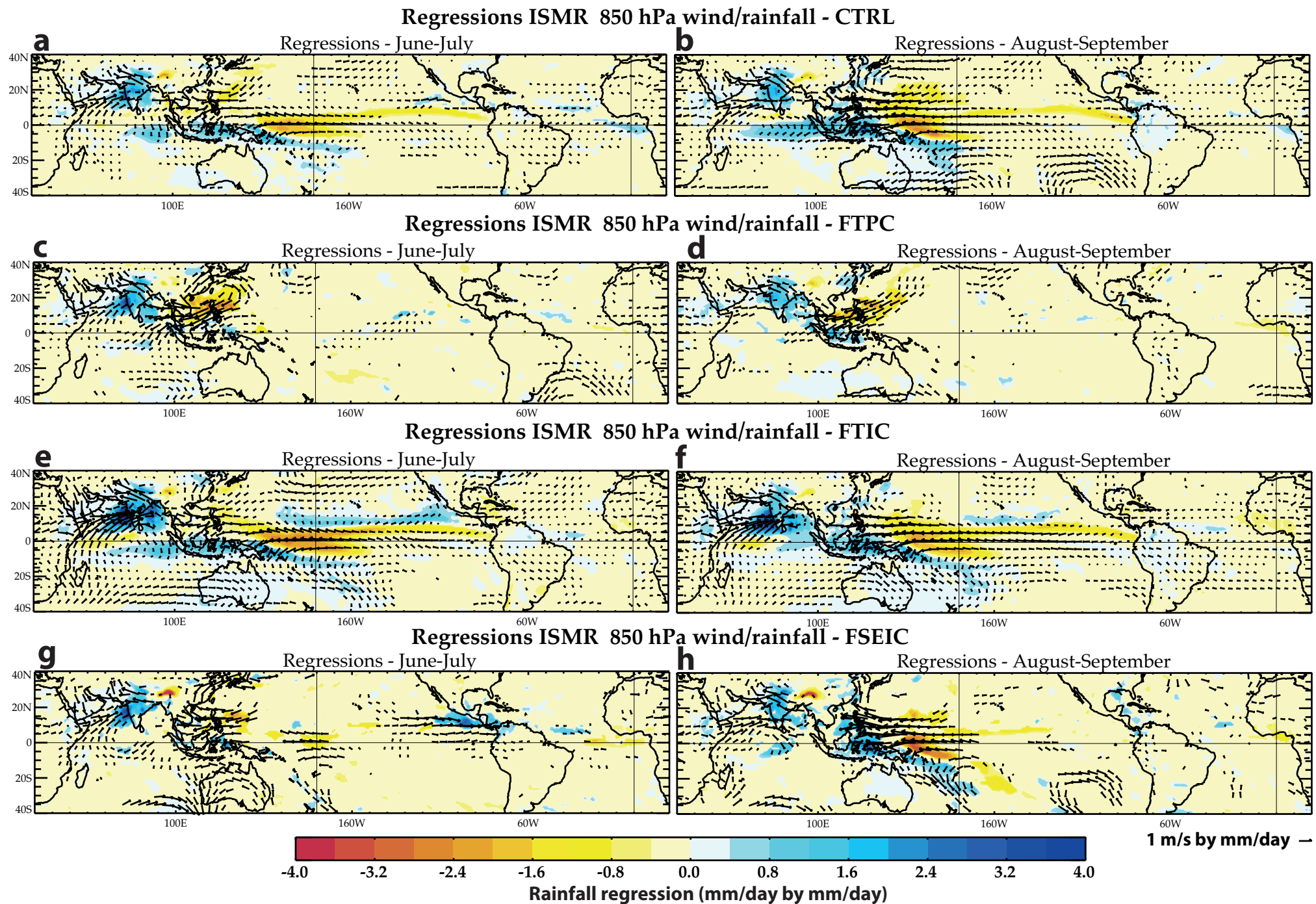


Figure 6: (a, b) June-July and August-September mean rainfall (shading) and 850-hPa wind (vectors) anomalies regressed against the ISMR index (e.g. JJAS ISM rainfall) in the CTRL experiment; (c, d) same as (a, b) but for the FTPC experiment; (e, f) same as (a, b) but for the FTIC experiment and (g, h) same as (a, b) but for the FSEIC experiment. Unit for the rainfall and 850-hPa wind regression coefficients are, respectively, in mm/day by mm/day and m/s by mm/day. Only rainfall and 850-hPa wind regression coefficients above the 95% significance confidence level according to a phase-scrambling bootstrap test (Ebisuzaki 1997) with 999 samples are shown.

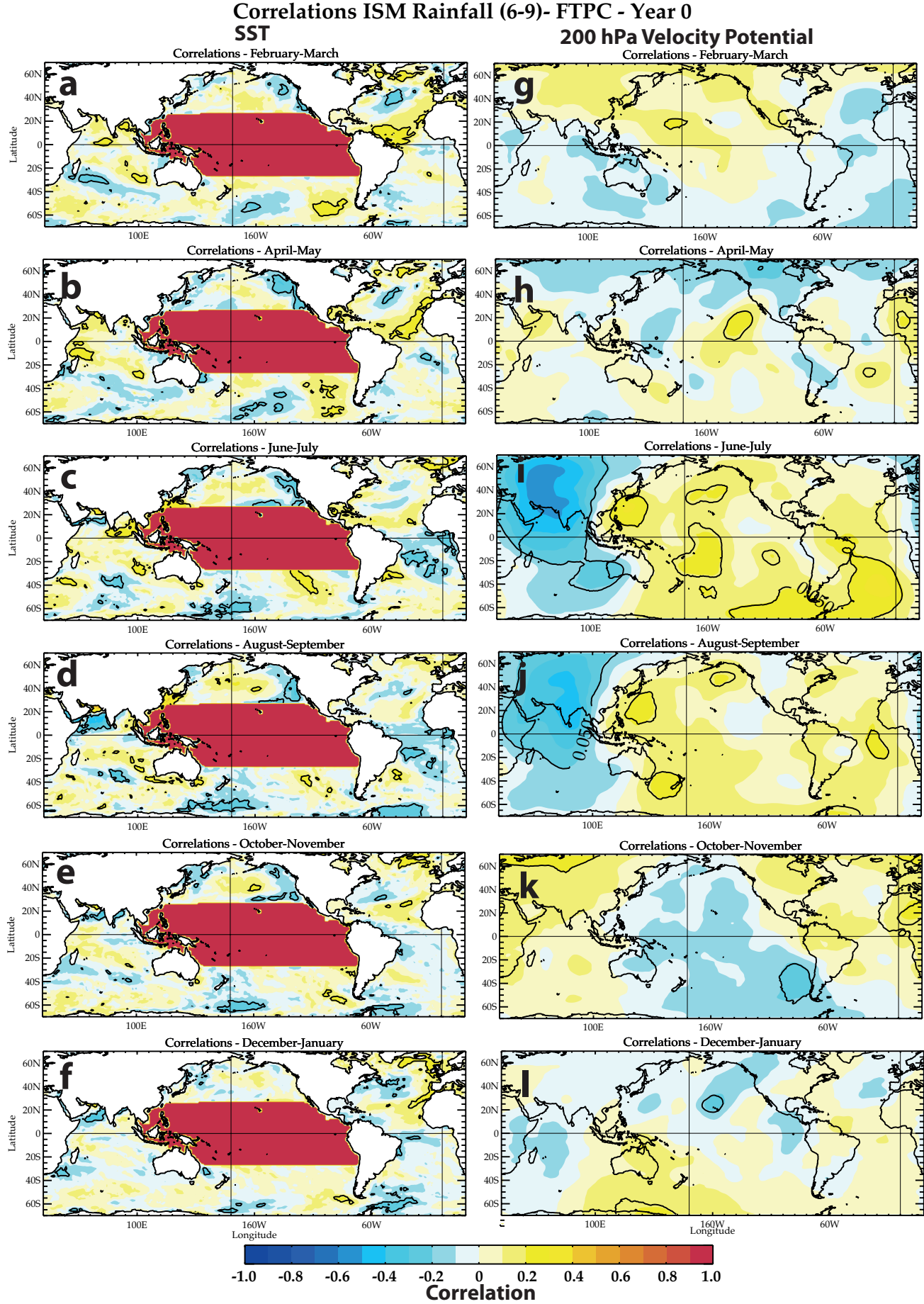


Figure 7: (a, b, c, d, e, f) correlation coefficients between the ISMR index (e.g. JJAS ISM rainfall) and bi-monthly SST anomalies from February-March to December-January of year 0 in the FTPC experiment. (g, h, i, j, k, l) same as (a, b, c, d, e, f) but for bi-monthly 200-hPa velocity potential anomalies. Correlation coefficients above the 95% significance confidence level according to a phase-scrambling bootstrap test (Ebisuzaki 1997) with 999 samples are contoured. In (a, b, c, d, e, f), correlation coefficients in the Pacific nudging domain are masked.

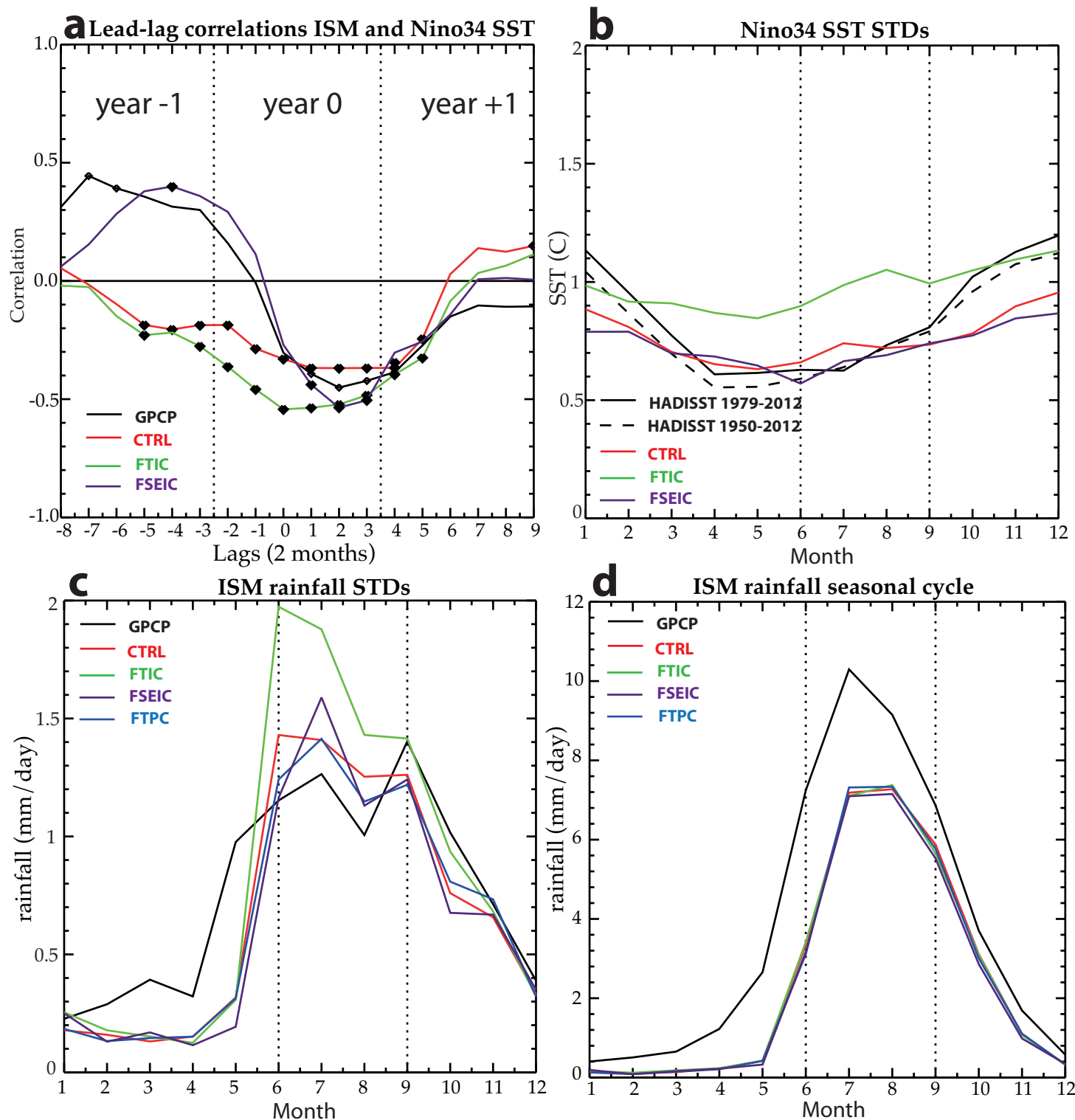


Figure 8: Same as Fig. 4, but for the FTIC and FSEIC experiments done with the SINTEX-F2 model. The results for the control (CTRL) and FTPC experiments performed with the SINTEX-F2 model are also displayed for comparison (only in panels **c** and **d** for FTPC).

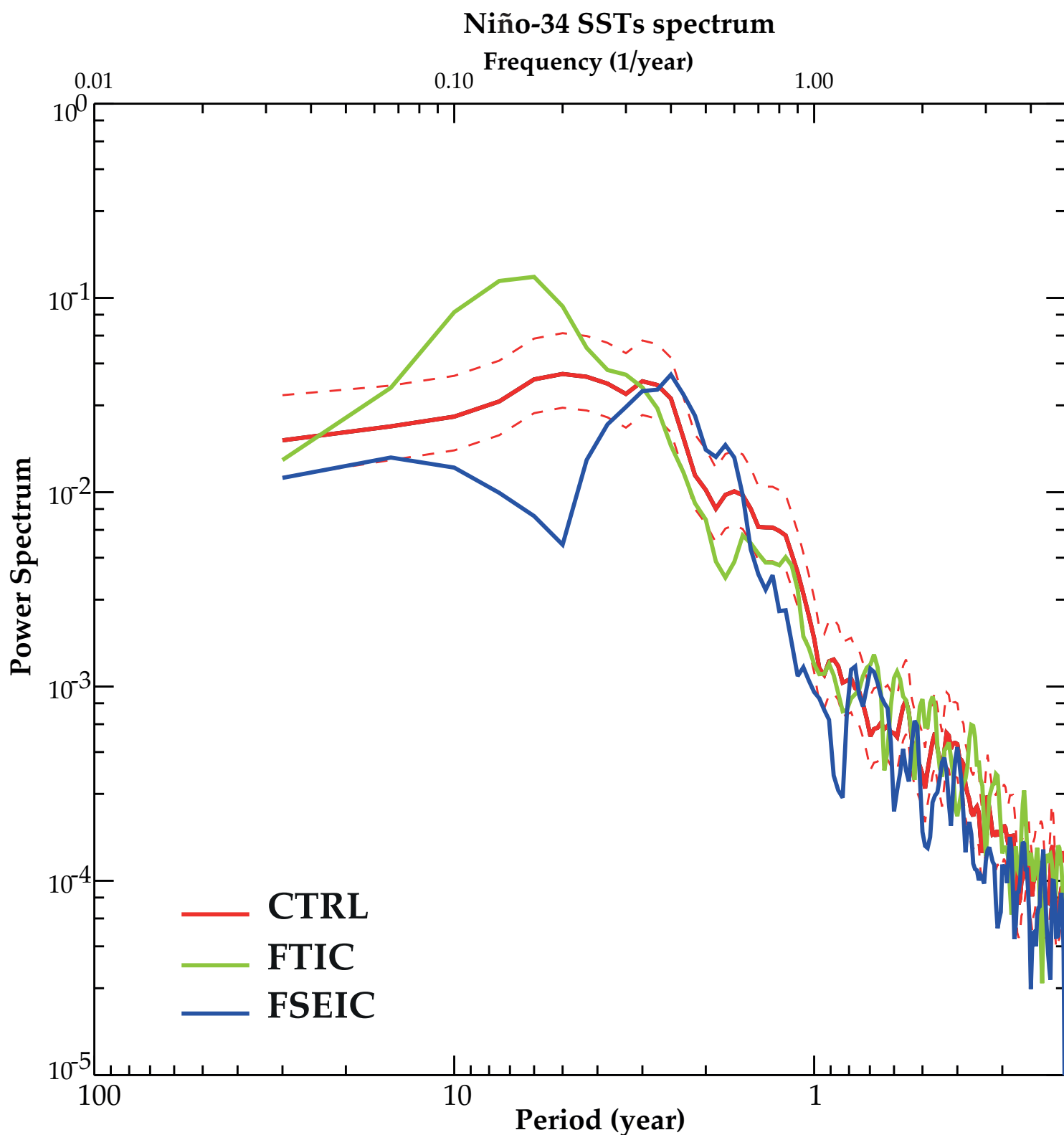


Figure 9: Power spectra of Niño-34 SST anomalies for CTRL (red), FTIC (green) and FSEIC (blue) experiments. The bottom axis is the period (unit: year), the left axis is variance (unit: $^{\circ}\text{C}^2$) and both axes are in logarithm scale. Dashed red curves show the point-wise 95% confidence limits for the Niño-34 SST spectrum estimated from the CTRL experiment.

Regressions Nino34 SST (12-1) SST - Year +1

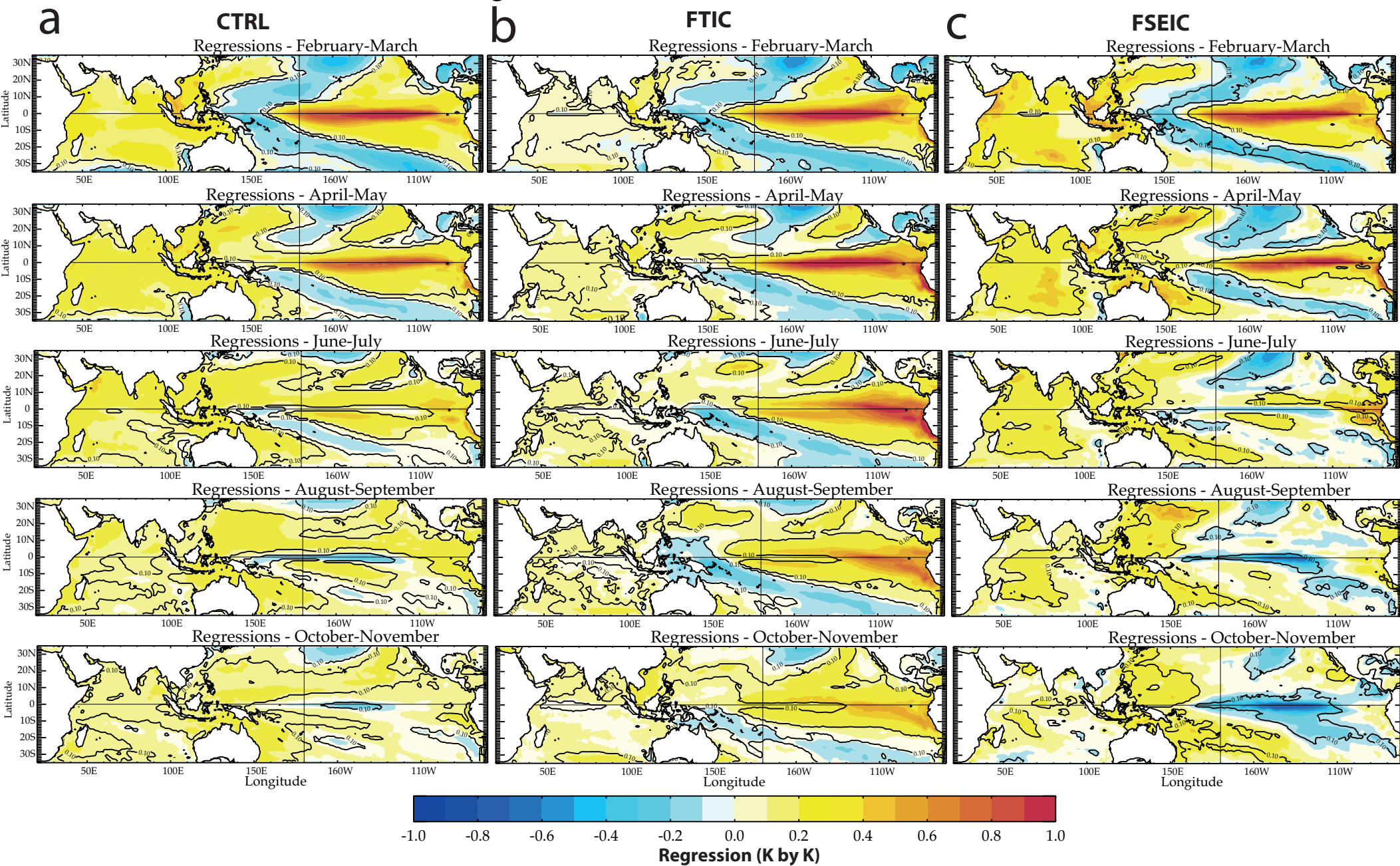


Figure 10: a) bi-monthly SST anomalies regressed against the December-January Niño-3.4 SST time series for the following February-March, April-May, June-July, August-September and October-November in the CTRL experiment; b) same as a) but for the FTIC experiment ; c) same as a) but for the FSEIC experiment. Unit for the SST regression coefficients is in K by K. Regression coefficients reaching the 10% significance level according to a phase-scrambling bootstrap test (Ebisuzaki 1997) with 999 samples are contoured.

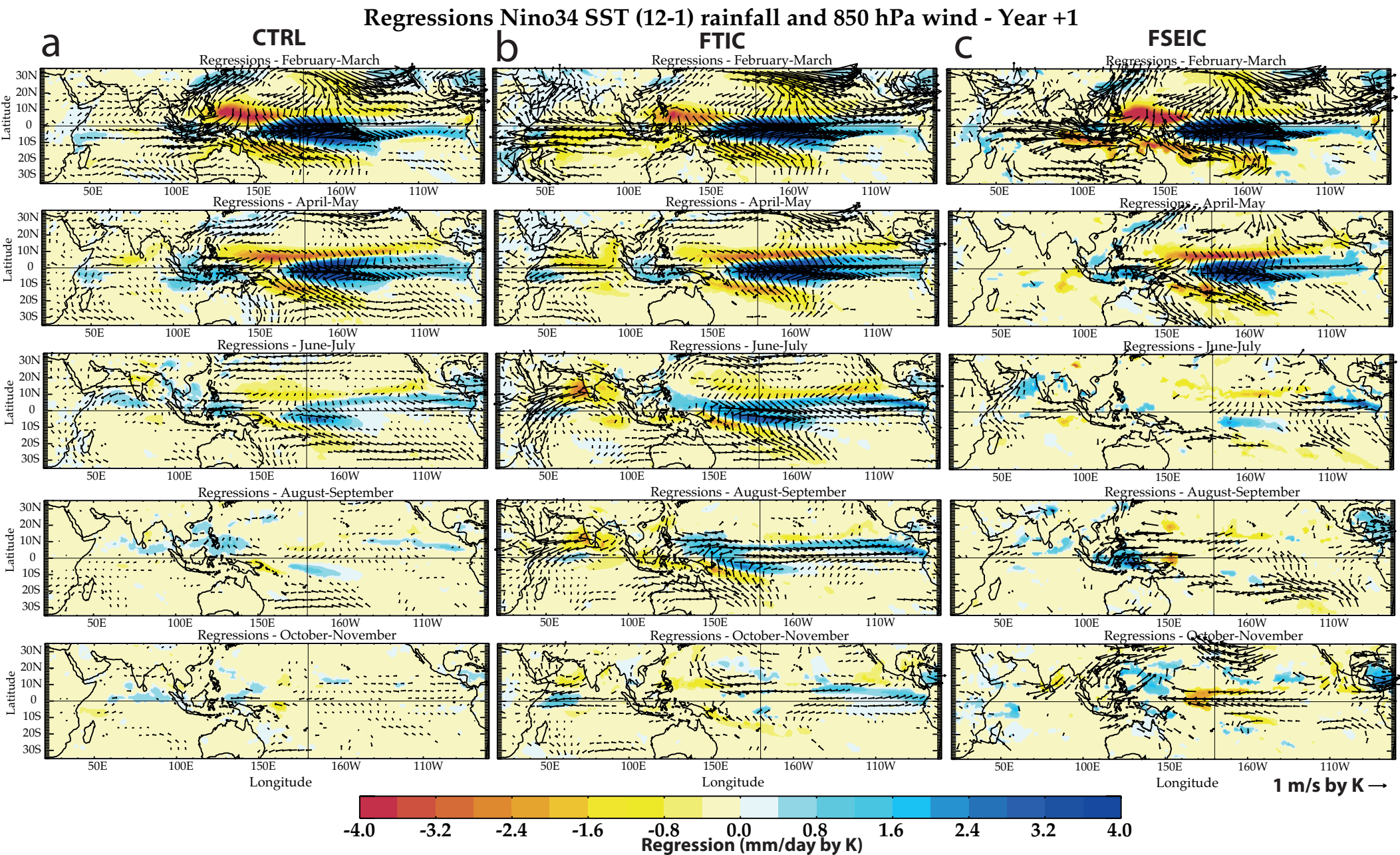


Figure 11: **a)** bi-monthly mean rainfall (shading) and 850-hPa wind (vectors) anomalies regressed against the December-January Niño-3.4 SST time series for the following February-March, April-May, June-July, August-September and October-November in the CTRL experiment; **b)** same as **a)** but for the FTIC experiment; **c)** same as **a)** but for the FSEIC experiment. Unit for the rainfall and 850-hPa wind regression coefficients are, respectively, in mm/day by K and m/s by K. Only rainfall and 850-hPa wind regression coefficients reaching the 10% significance level according to a phase-scrambling bootstrap test (Ebisuzaki 1997) with 999 samples are shown.

Regressions Nino34 SST (12-1) depth of 20°C isotherm - Year +1

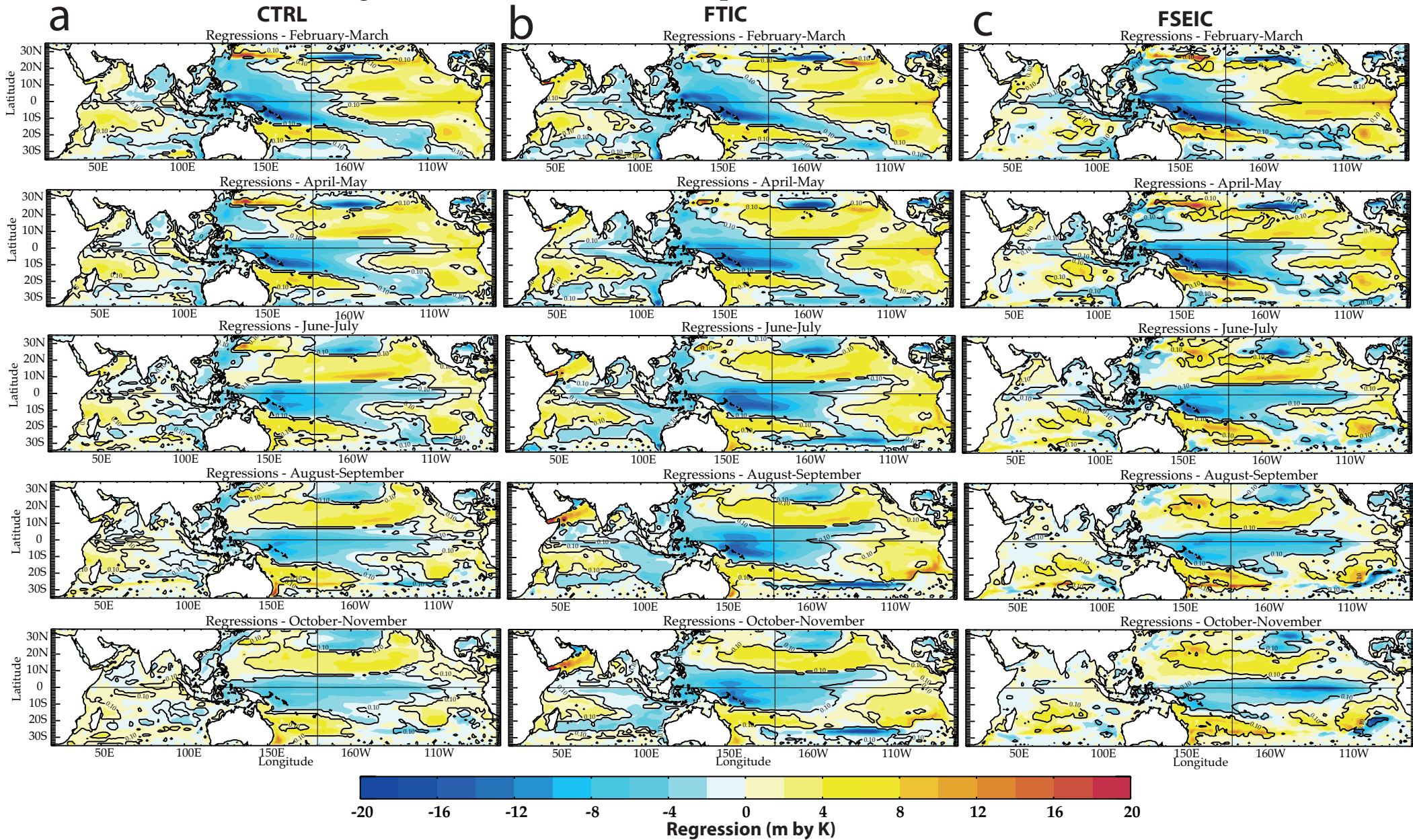


Figure 12: **a)** bi-monthly mean 20°C isotherm depth (a proxy for thermocline depth) anomalies regressed against the December-January Niño-3.4 SST time series for the following February-March, April-May, June-July, August-September and October-November in the CTRL experiment; **b)** same as **a)** but for the FTIC experiment ; **c)** same as **a)** but for the FSEIC experiment. Unit for the 20°C isotherm depth regression coefficients is in m by K. Regression coefficients reaching the 10% significance level according to a phase-scrambling bootstrap test (Ebisuzaki 1997) with 999 samples are contoured.

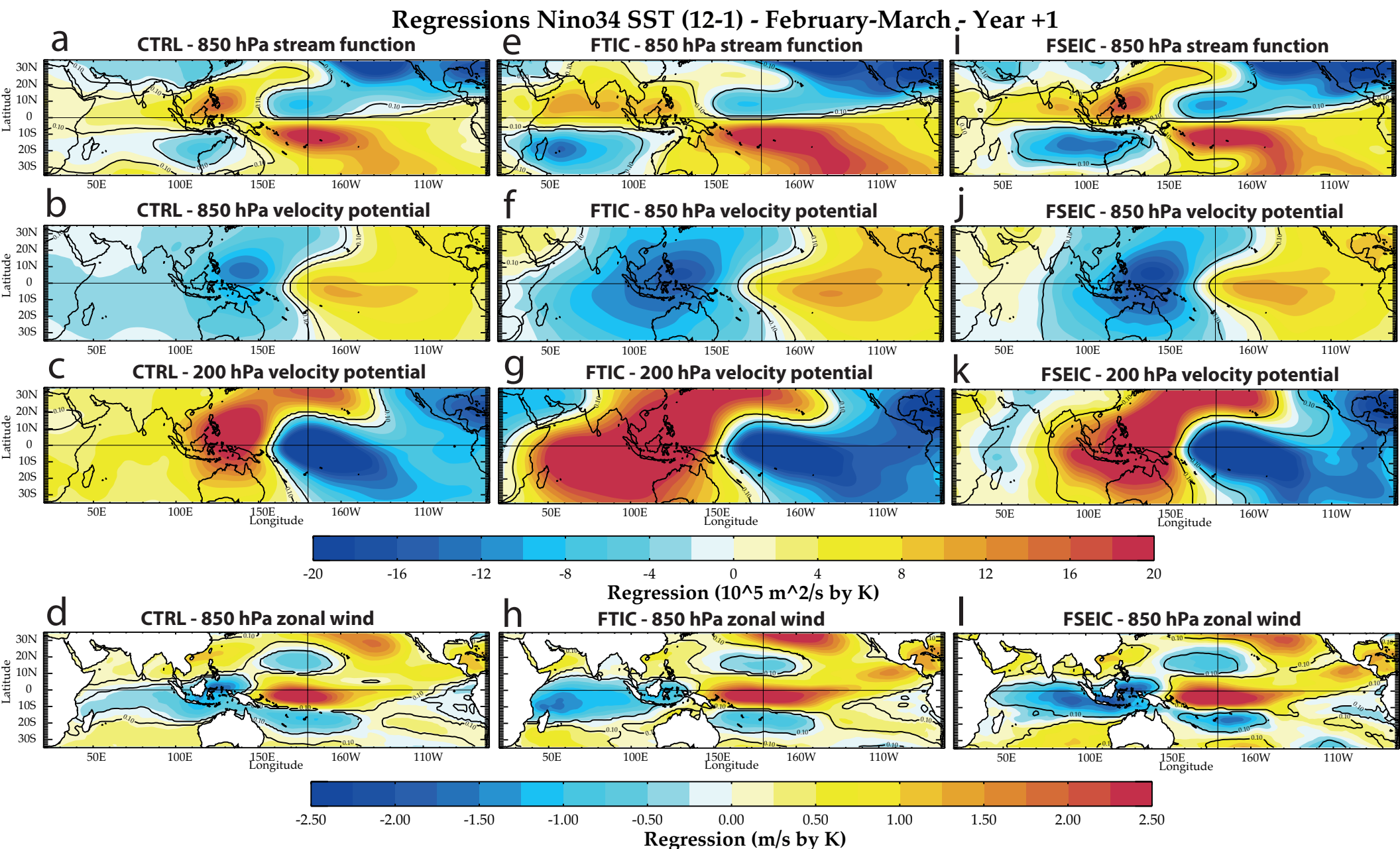


Figure 13: (a, b, c, d) February-March 850-hPa stream function, 850-hPa velocity potential, 200-hPa velocity potential and 850-hPa zonal wind anomalies regressed against the preceding December-January Niño-3.4 SST time series in the CTRL experiment; (e, f, g, h) same as (a, b, c, d) but for the FTIC experiment; (i, j, k, l) same as (a, b, c, d) but for the FSEIC experiment. Units for the stream function and velocity potential regression coefficients are in $10^5 \text{ m}^2 \text{ s}^{-1} \text{ by K}$ and for 850-hPa zonal wind in $\text{m s}^{-1} \text{ by K}$. Regression coefficients reaching the 10% significance level according to a phase-scrambling bootstrap test (Ebisuzaki 1997) with 999 samples are contoured.

Regressions Nino34 SST (12-1) - 200 hPa velocity potential - Year +1

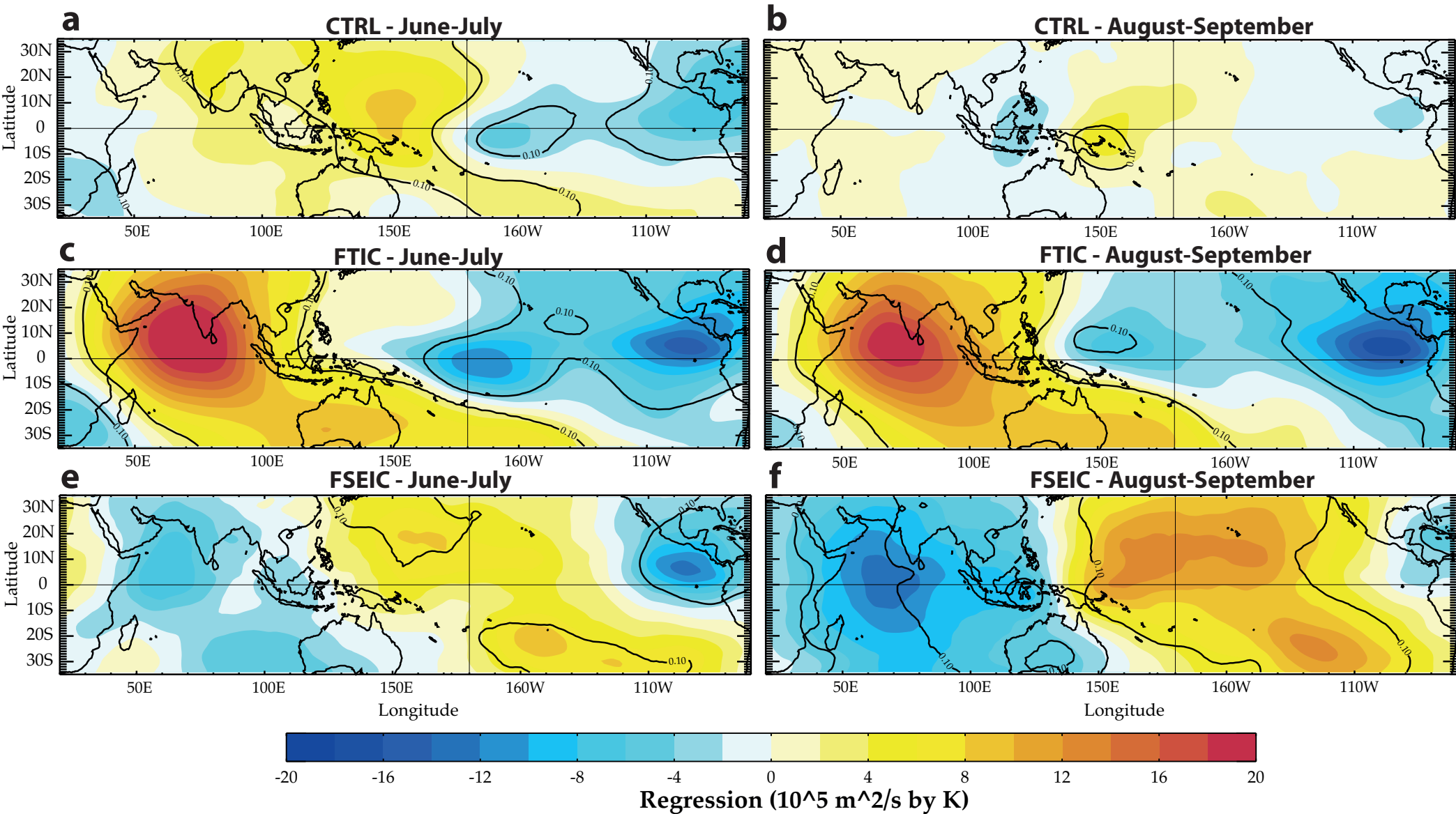


Figure 14: (a, b) June-July and August-September 200-hPa velocity potential anomalies regressed against the preceding December-January Niño-3.4 SST time series in the CTRL experiment; (c, d) same as (a, b) but for the FTIC experiment; (e, f) same as (a, b) but for the FSEIC experiment. Units for the velocity potential regression coefficients are in $10^5 \text{ m}^2 \text{ s}^{-1} \text{ by K}$. Regression coefficients reaching the 10% significance level according to a phase-scrambling bootstrap test (Ebisuzaki 1997) with 999 samples are contoured.

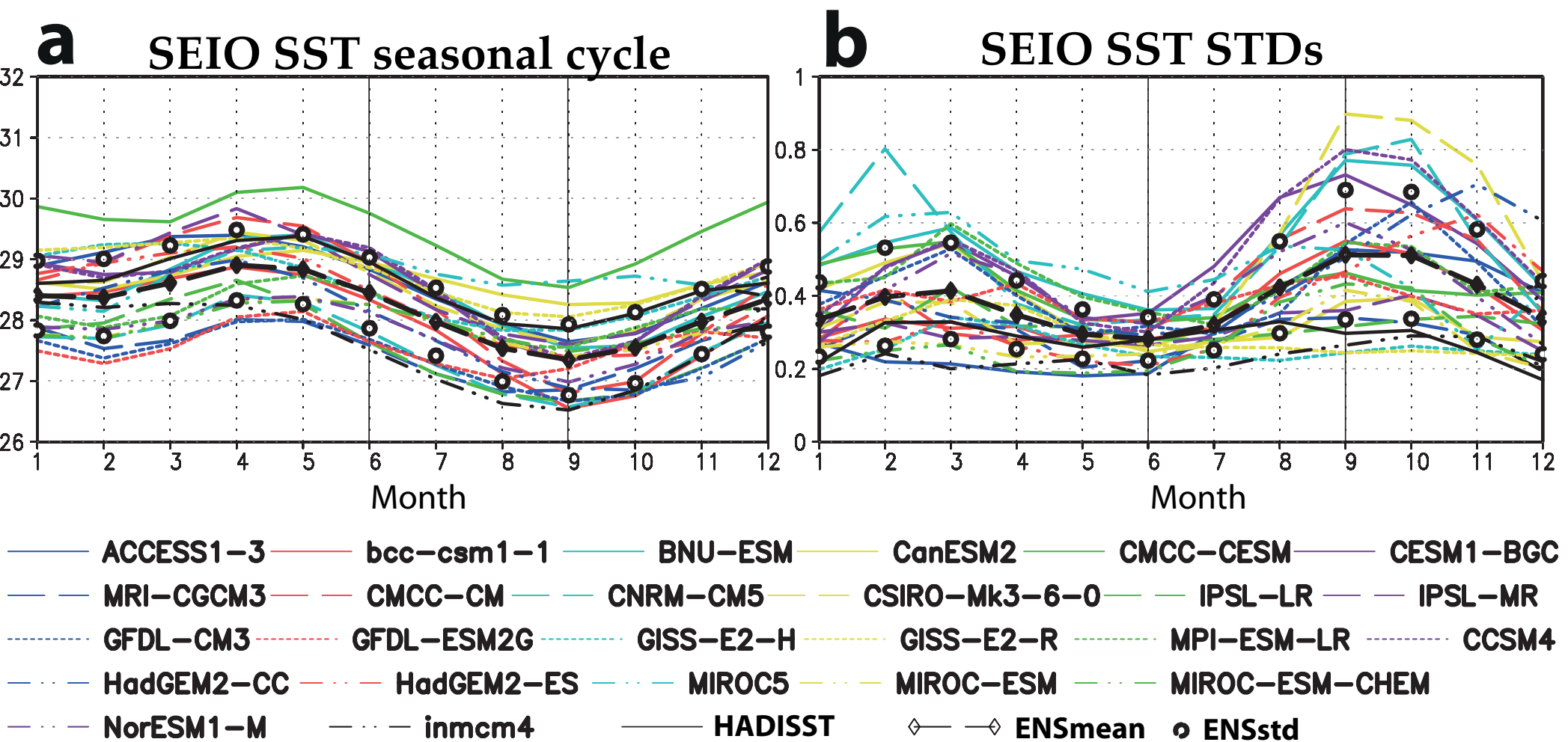
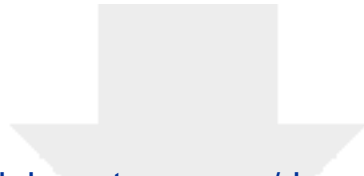


Figure 14: **a)** Monthly means of the SEIO (90°E - 115°E and 0°S - 10°S ; unit: $^{\circ}\text{C}$) SST time series from HadISST1.1 dataset and the historical runs of 25 CMIP5 models; **b)** Monthly standard deviations of the SEIO SST time series from HadISST1.1 dataset and the historical runs of 25 CMIP5 models. All observed and simulated statistics are estimated from the period 1950-2000. The ensembles mean and spread across the CMIP5 models are also displayed. The spread is computed as the ensemble mean plus and minus the ensemble standard deviation (thick black circles in panels **a** and **b**).

Table 1

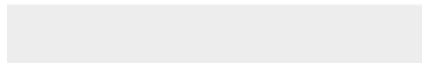
Name	CTRL	FTPC	FTIC	FSEIC	FTPC-obs
Correction area	None	Pacific Ocean coast to coast 25°S-25°N	Indian Ocean coast to coast 25°S-30°N	Indian Ocean 90°E to coast 0°S-10°S	Pacific Ocean coast to coast 25°S-25°N
Smoothing area	None	30°S-25°S 25°N-30°N	30°S-25°S	85°E-90°E, 115°E-120°E 15°S-10°S 0°-5°N	30°S-25°S 25°N-30°N
SST data	None	CTRL	CTRL	CTRL	OISSTv2
Time duration (Year)	210	110	110	60	50

Table 1: Summary of the numerical experiments with their main characteristics, including length, nudging domain and SST climatology used for the nudging in the Indian or Pacific oceans decoupled experiments. The nudged experiments are the Forced Tropical Pacific Climatology (FTPC) run, the Forced Tropical Indian Climatology (FTIC) run, the Forced South-East Indian Climatology (FSEIC) run and, finally, the Forced Tropical Pacific observed Climatology (FTPC-obs) run. See text for more details. For the FTPC and FTPC-obs experiments only ocean grid-points in the Pacific are included in the correction or smoothing areas and, similarly, for the FTIC and FSEIC experiments for their respective domains. The different correction domains are also displayed in Figure 1b-d. The observed SST climatology used in the FTPC-obs experiment is derived from the AVHRR only daily Optimum Interpolation SST version 2 (OISSTv2) dataset for the 1982–2010 period (Reynolds et al. 2007).



[Click here to access/download](#)

Electronic Supplementary Material
TableS1.doc





Click here to access/download
Electronic Supplementary Material
FigureS1_revised.eps

